Shared dynamical features of smooth- and rough-wall boundary-layer turbulence

R. L. Ebner[1,‡], Faraz Mehdi[2] and J. C. Klewicki[3,4,†]

[1]The MITRE Corporation, Bedford, MA 01730, USA

[2]Light Industrial Systems, Hypertherm Inc, Lebanon, NH 03766, USA

[3]Department of Mechanical Engineering, University of New Hampshire, Durham, NH 03824, USA

[4]Department of Mechanical Engineering, University of Melbourne, Victoria 3010, Australia

The structure of smooth- and rough-wall turbulent boundary layers is investigated using existing data and newly acquired measurements derived from a four element spanwise vorticity sensor. Scaling behaviours and structural features are interpreted using the mean momentum equation based framework described for smooth-wall flows by Klewicki (*J. Fluid Mech.*, vol. 718, 2013, pp. 596–621), and its extension to rough-wall flows by Mehdi *et al.* (*J. Fluid Mech.*, vol. 731, 2013, pp. 682–712). This framework holds potential relative to identifying and characterizing universal attributes shared by smooth- and rough-wall flows. As prescribed by the theory, the present analyses show that a number of statistical features evidence invariance when normalized using the characteristic length associated with the wall-normal transition to inertial leading-order mean dynamics. On the inertial domain, the spatial size of the advective transport contributions to the mean momentum balance attain approximate proportionality with this length over significant ranges of roughness and Reynolds number. The present results support the hypothesis of Mehdi *et al.*, that outer-layer similarity is, in general, only approximately satisfied in rough-wall flows. This is because roughness almost invariably leaves some imprint on the vorticity field; stemming from the process by which roughness influences (generally augments) the near-wall three-dimensionalization of the vorticity field. The present results further indicate that the violation of outer similarity over regularly spaced spanwise oriented bar roughness correlates with the absence of scale separation between the motions associated with the wall-normal velocity and spanwise vorticity on the inertial domain.

Key words: turbulence theory, turbulent boundary layers, turbulent flows

---

1. Introduction

Surface roughness significantly influences the dynamical structure of many technologically important wall-bounded turbulent flows, e.g. Raupach, Antonia & Rajagopalan ([1991](#)). Unravelling the complicated physics by which roughness alters

---

† Email address for correspondence: joe.klewicki@unh.edu

‡ The author's affiliation with The MITRE Corporation is provided for identification purposes only, and is not intended to convey or imply MITRE's concurrence with, or support for, the positions, opinions or viewpoints expressed by the author.

the dynamics of the turbulence (relative to the smooth-wall case), and in turn, describing the resulting mean flow properties, constitute substantial challenges to practical engineering prediction and design. Here the apparent complexity and accompanying challenges seem largely attributable to the expansive variety of roughness shapes and sizes that might be encountered.

There are, however, valid reasons to suspect that another part of the apparent challenge connects to the paradigm traditionally used to guide rough-wall data analysis. Namely, an emerging body of evidence supports perspectives that, in important aspects, diverge from the traditional paradigm. These perspectives derive from a different yet well-founded framework that incorporates unifying mathematical and physical concepts for describing time-averaged dynamics; including their characterization and scaling in both smooth- and rough-wall flows. This framework follows from consideration of the mean differential statement of dynamics, and analyses within this framework lead to findings that are consistent with observed dependencies on roughness and Reynolds number. The broad purpose of the present study is to advance more detailed inquiry within the context of this framework. This is accomplished by clarifying important characteristics of the inertial mechanism of momentum transport, and by doing so, exposing dynamically relevant properties that are shared by, and thus potentially universal to, both smooth- and rough-wall flows.

1.1. *Pertinent aspects of rough-wall structure*

The present study considers incompressible turbulent boundary-layer flow over a nominally flat surface upon which there is a dynamically significant roughness. Herein the coordinate x, denotes the main flow direction and the positive y coordinate is normal to the average plane of the surface. The friction velocity is denoted by $u_\tau (= \sqrt{\tau_{wall}/\rho})$, where τ_{wall} is the mean wall shear stress, and ρ is the mass density. Velocity components in the x and y directions are respectively given by variants of u and v, with upper case letters denoting mean quantities, and lower case letters denoting zero-mean fluctuating quantities. Angle brackets denote the time average, a superscript + indicates normalization by ν and u_τ, and a prime denotes the root-mean-square (r.m.s.) of a fluctuating quantity. The boundary-layer thickness is given by δ, and the equivalent sand grain roughness is given by k_s. Excluding y locations below the roughness crests, the flows of interest are two-dimensional in the mean and have no mean pressure gradient.

Townsend's similarity hypotheses (Townsend 1976) attaches a universal statistical structure to the outer region of smooth- and rough-wall flows, and thus has relevance to the present study. Numerous experiments lend support to this hypothesis, but such experiments are most commonly characterized by a randomly distributed roughness that is small relative to δ, e.g. Raupach *et al.* (1991), Jiménez (2004), Flack, Schultz & Shapiro (2005). In addition, an apparent ambiguity of Townsend's notion is in the wall-normal location where outer similarity begins to take hold. Here, the roughness sublayer concept is often invoked, but the specification of this sublayer is equally vague, e.g. ~ 3–$5k_s$ above the roughness. When the roughness is relatively large, geometrically organized or both, a significant number of experiments evidence deviations from outer similarity. A prevalently studied flow of this kind is over spanwise aligned square bars or circular rods having a streamwise spacing of about 8 bar widths or rod diameters, e.g. Krogstad & Antonia (1999), Djenidi *et al.* (2008), Volino *et al.* (2011).

Relatively recent measurements provide some clarifying details regarding the validity or breakdown of outer similarity. At very high Reynolds number ($\delta^+ \simeq 10^6$) (Priyadarshana *et al.* 2007) observed that near wall statistics of flows with large roughness ($k_s^+ \simeq 300$), i.e. well within the fully rough classification ($k_s^+ \gtrsim 70$), exhibited properties that were surprisingly similar to those found in smooth-wall flow. In a similar vein, for nominally fixed k_s/δ, Efros & Krogstad (2011) found a diminishing violation of outer similarity with increasing δ^+. The observations by Hong, Katz & Schultz (2011) suggest a direct roughness effect on the scale of the vortical motions. For the organized three-dimensional roughness they explored, the roughness signature was not only seen near the wall, but throughout the boundary layer. Volino *et al.* (2011) investigated causal factors leading to the breakdown of outer similarity; documenting flow properties over square bars of different sizes and regular arrays of rectangular elements; essentially square bars with sections removed at regular spanwise intervals. Their results suggest that the geometric regularity of the roughness has a significance comparable to that of roughness size relative to promoting a violation of Townsend's hypothesis. This would seem to bear some consistency with observations that even small organized roughness can significantly influence the overall flow structure (Monty *et al.* 2011*a*). As part of a broader effort to characterize the mean force structure of rough-wall flows, Mehdi *et al.* (2013) adopted the methodology used by Wei *et al.* (2005) in smooth-wall flows. Here the relative magnitudes of the terms appearing in the mean momentum equation were used to identify the leading-order balances of terms, as well as the sub-domains where these balances exist. Relative to Townsend's hypothesis, Mehdi *et al.* (2013) evidenced that, if it holds, outer similarity begins to hold at the wall-normal location where the mean viscous force loses leading-order importance. The physics and scaling behaviours associated with this concept are central to the present study, and thus are now discussed in greater detail.

1.2. *Wall-normal transition to inertial mean dynamics*

To within Prandtl's boundary-layer approximation the inner-normalized mean momentum equation for these flows is

$$\left(U^+ \frac{\partial U^+}{\partial x^+} + V^+ \frac{\partial U^+}{\partial y^+} \right) + \frac{\partial \langle uv \rangle^+}{\partial y^+} = \frac{\partial^2 U^+}{\partial y^{+2}}, \tag{1.1}$$

where $\langle uv \rangle^+$ is commonly called the Reynolds stress. Mean inertia (*MI*) is represented by the terms inside the parentheses in (1.1). The remaining term on the left represents the net mean effect of the turbulent inertia (*TI*). The term on the right of (1.1) is the mean viscous force (*VF*). Equation (1.1) is valid for both smooth- and rough-wall flows, under the recognition that the statistical structure of the flow will, as a function of specific roughness geometry, become heterogeneous in the immediate vicinity of the roughness elements. In this region, highly organized roughness (e.g. two-dimensional bars) may generate detectable zones of streamwise pressure gradient that withstand time averaging.

As clarified through examination of the ratio, *VF*/*TI*, not all of the terms in (1.1) are leading order everywhere between $y = 0$ and $y = \delta$. A structural feature of particular interest is the y position where the leading-order balance of terms becomes $MI = TI$. Below this position the *VF* term is leading order, and for all locations above this position the leading mean dynamics are inertial. In smooth-wall flows, this transition
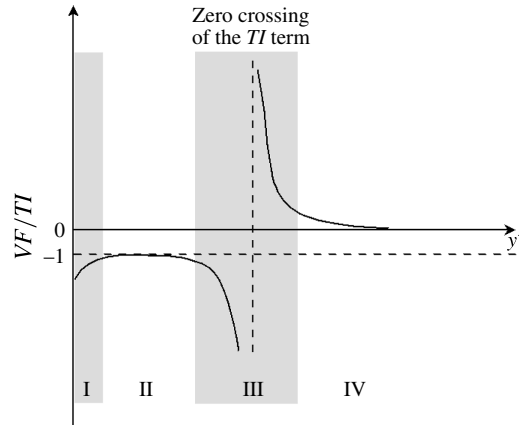
FIGURE 1. Sketch of the ratio of the ratio of terms, *VF/TI*, appearing in (1.1) for any given Reynolds number. Note that in rough-wall flow layer I is not present.

to inertially dominated mean dynamics occurs at $y = O(\sqrt{\nu\delta/u_\tau})$ (Wei *et al.* 2005; Fife *et al.* 2009). More generically, this locates the outer edge of layer III (inner edge of layer IV) of the four-layer structure that describes the leading terms in (1.1) for varying y (Wei *et al.* 2005; Mehdi *et al.* 2010). This structure is depicted in the sketch of figure 1. For smooth-wall flow, layer IV starts at a position $y \simeq 2.6\sqrt{\nu\delta/u_\tau}$ from the wall. Recent observations that the logarithmic mean velocity and streamwise velocity variance profiles start near $y = 3\sqrt{\nu\delta/u_\tau}$ (Marusic *et al.* 2013; Vincenti *et al.* 2013), are explained by the inertial domain onset at $y \simeq 2.6\sqrt{\nu\delta/u_\tau}$ ($y^+ \simeq 2.6\sqrt{\delta^+}$). In rough-wall flows (Mehdi *et al.* 2013) evidenced that this location is physically dictated by the relative scale separation between the inner, roughness and outer lengths, and thus is inherently a property of both k_s^+ and δ^+ (see below). Consistent with this, Meyers *et al.* (2015) show that wall pressure spectra in rough-wall flows evidence invariance over an intermediate range of frequencies when these relative scale separations are incorporated in the normalization.

Mehdi *et al.* (2013) (hereafter MKW13) show that layers II–IV are generically preserved in rough-wall flows, while layer I is obliterated for all but diminishing k_s^+. (As in MKW13, the equivalent sand grain roughness, k_s, is used herein as a single-length characterization of the roughness.) Using new and existing rough-wall measurements, MKW13 developed the semi-empirical relations (1.2) for y_m. Because it always resides within layer III, y_m is a useful surrogate for the onset of the inertial domain (Mehdi *et al.* 2013; Morrill-Winter & Klewicki 2013; Chin *et al.* 2014). Equations (1.2) indicate that the transition to inertial mean dynamics occurs at a position that depends on weighted contributions from the roughness length, k_s, the viscous length, ν/u_τ and the outer length, δ. These weightings are associated with the relative scale separations between ν/u_τ, k_s, y_m and δ.

$$y_m \simeq \begin{cases} 0.80(\nu/u_\tau)^{0.25}\, k_s^{0.46}\, \delta^{0.29}, & y_m/k_s < O(1), \\ 2.14(\nu/u_\tau)^{0.28}\, k_s^{0.50}\, \delta^{0.22}, & y_m/k_s \approx O(1), \\ 0.89(\nu/u_\tau)^{0.36}\, k_s^{0}\, \delta^{0.64}, & y_m/k_s > O(1). \end{cases} \qquad (1.2)$$

Relations (1.2) represent the best fit to functions of the form

$$y_m = C(\nu/u_\tau)^a\, k_s^b\, \delta^c, \qquad (1.3)$$

and were determined using data that cover a broader range of k_s^+ and δ^+ than considered herein. As required, the exponents are constrained by $a + b + c = 1$. In accord with observations at large k_s^+ and very large δ^+, (1.2) are consistent with the emergence of new roughness regimes with increasing δ^+ (Priyadarshana *et al.* 2007). These are associated with the increasing variety of relative scale separation conditions between ν/u_τ, k_s, y_m, and δ that can arise when the overall scale separation (as quantified by δ^+) becomes large. Here the generic existence of layer II is particularly relevant, since the presence of a leading-order viscous influence above a so-called fully rough surface diverges from the prevalent perspective that the mean viscous force is negligible for all y locations above such a surface. The fully rough condition indicates that pressure (form) drag around the roughness elements is, on average, dominant. Traditional thinking links this condition to inertial mean dynamics in the flow above the roughness. The findings of MKW13, and herein, indicate that this is generically not the case.

1.3. *Modified structure of mean dynamics*

While the layer II–IV structure is qualitatively preserved for rough-wall flows, it is rational to expect the underlying momentum transport mechanisms to be significantly modified, and that such modifications ought to be detectable in the characteristic length and time scales of the relevant motions. One intent of the present study is to investigate the veracity of this hypothesis, while another aim is to clarify the manner by which such influences (if detectable) are attributable to roughness. Issues relevant to this aim are brought to light by qualitatively comparing the physics associated with the mean dynamical structure in smooth- and rough-wall flows.

1.3.1. *Smooth-wall flow physics*

Figure 2 depicts momentum and vorticity field behaviours for the smooth-wall boundary layer that retain consistency with the mean dynamics. Features associated with momentum transport are denoted on the right of figure 2. Herein the focus is on the region beyond layer III, where the leading-order mean dynamics are inertial. On this domain, the present analytical framework reveals that (1.1) admits a specific invariance structure, and that this structure is consistent with the emergence (as $\delta^+ \to \infty$) of distance from the wall scaling and a logarithmic mean velocity profile, e.g. Klewicki (2013*a*). Other features documenting the apparent success of this theory are mentioned in §2 below.

The left side of figure 2 shows the associated vorticity field behaviours. Very near the wall (layer I), the instantaneous vorticity vector primarily meanders in the (x, z) plane (Klewicki *et al.* 1990). For y increasing into layer II, however, the smooth-wall vorticity field undergoes a rapid three-dimensionalization associated with vorticity stretching and reorientation. Here, a strong transfer from the mean to the fluctuating enstrophy coincides with a precipitous decrease in the mean vorticity magnitude, $|\Omega_z| \simeq |-\partial U/\partial y|$ (Klewicki 2013*b*). This occurs in the region $y^+ \lesssim 40$, and results in $|\Omega_z|$ diminishing to values less than the r.m.s. of the spanwise vorticity fluctuations, ω_z', as well as an equalization of ω_x' and ω_y' with ω_z' (Klewicki 1997). Indeed, it is generally not well recognized that starting very close to the wall ($y^+ \simeq 20$), and essentially independent of δ^+, the instantaneous spanwise vorticity regularly undergoes sign reversals (Klewicki *et al.* 1990; Metzger & Klewicki 2001).

The leading-order competition between the *TI* and *VF* terms in (1.1) persists in layer II up to a wall-normal position that, with increasing δ^+, becomes much
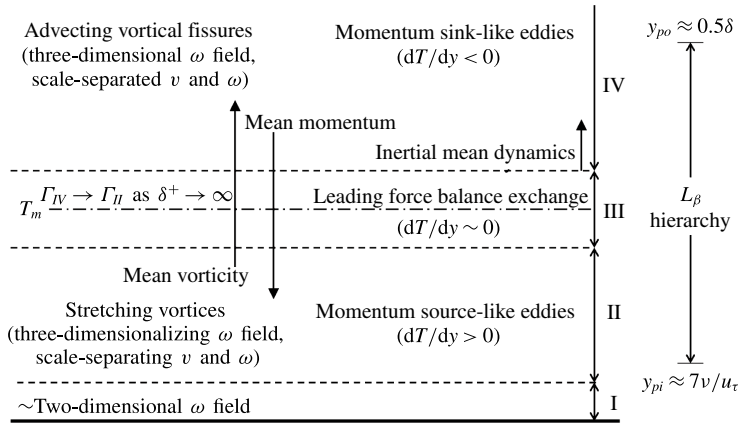
FIGURE 2. A depiction of the mean dynamics and vorticity field processes consistent with the mean similarity structure of smooth-wall turbulent flows, adapted from Klewicki (2013*b*).

larger than the thickness of the traditional buffer layer ($y^+ \simeq 40$). In layer II there is also an increasing scale separation between the motions characteristic of the velocity and vorticity fields (Morrill-Winter & Klewicki 2013). Commensurate with vorticity stretching, layer II scale separation is largely caused by a reduction in the characteristic size of the vortical motions. With the onset of the inertial layer the vorticity increasingly concentrates in slender vortical fissures that bound zones of approximately uniform momentum, as first observed by Meinhart & Adrian (1995). Here the predominant scale separation mechanism shifts to a spatial dispersion of the vortical motions (via advective transport) that are generated in layer II by the stretching and reorientation processes just described (Klewicki 2013*b*; Morrill-Winter & Klewicki 2013; Chin *et al.* 2014).

1.3.2. *Rough-wall flow physics*

In rough-wall flows, the physical processes represented in figure 2 are postulated to still be operative. In this case, however, the geometric organization of the vorticity field is at least partially caused by the roughness, and this roughness signature generally survives into the outer region. Such effects are expected to modify the scale separated dynamics characteristic of outer similarity, and the associated structural features of uniform momentum zones segregated by narrow vortical fissures. The present measurements partially assess the validity of this depiction, and its connection to violations of outer-layer similarity.

Understanding the *TI* term in (1.1) is aided by the identity

$$TI = -\frac{\partial \langle uv \rangle^+}{\partial y^+} = \langle v\omega_z \rangle^+ - \langle w\omega_y \rangle^+ + \frac{\partial}{\partial x^+}(\langle v^2 \rangle^+ + \langle w^2 \rangle^+ - \langle u^2 \rangle^+). \quad (1.4)$$

The last term in (1.4) is identically zero in channel and pipe flow, and negligible under the boundary-layer approximation. Thus, the *TI* term is well approximated by the difference of the indicated velocity vorticity correlations, especially as $\delta^+ \rightarrow \infty$. These two contributions sum to zero where $TI = 0$, or equivalently, where $-\langle uv \rangle^+$ attains its maximum, y_m^+. From smooth-wall flow studies it is known that for $y^+ < y_m^+$ the largest

contribution to *TI* comes from $\langle w\omega_y \rangle^+$, and for $y^+ > y_m^+$ the largest contribution is $\langle v\omega_z \rangle^+$ (Klewicki 2013*b*; Morrill-Winter & Klewicki 2013; Chin *et al.* 2014). These studies largely support the physical interpretation of Tennekes & Lumley (1972) that the $w\omega_y$ motions are associated with change-of-scale effects resultant from vorticity stretching, and that the $v\omega_z$ motions are associated with wall-normal advective vorticity transport. The present measurements examine behaviours pertaining to the $\langle v\omega_z \rangle^+$ term. Here the decomposition of (1.4) is particularly appropriate for the study of scale separation effects, since the characteristic wavelengths respectively associated with the velocity and vorticity naturally migrate to disparate values with increasing δ^+ (Morrill-Winter & Klewicki 2013). In the rough-wall case, however, the scales of motion underlying the correlations in (1.4) are influenced by both the roughness imposed scales and the scale separation reflected in the value of δ^+.

1.4. *Objectives*

The present objectives are directed toward clarifying dynamical effects associated with the combined influences of roughness and Reynolds number and, when possible, identifying physical mechanisms and scaling behaviours that are shared between smooth- and rough-wall flows. Here, special attention is paid to the connections between structural features, and the onset and extent of the inertial domain. Properties of turbulent momentum transport are characterized using statistics and spectra associated with the $\langle v\omega_z \rangle^+$ term in (1.4) for significant variations in k_s^+ and δ^+.

The next section briefly describes elements of the present theory relevant to developing a scaling framework that generically applies to both smooth- and rough-wall flows. This framework adds further focus to the present aims. Descriptions of the experiments and the data analysis methods follow in §§ 3 and 4, respectively. Section 5 presents and describes the experimental results. Conclusions regarding these results are drawn and discussed relative to the theoretical framework in § 6.

2. Elements of the theoretical framework

A framework for describing the dynamical structure and scaling of both smooth- and rough-wall flows is now outlined.

2.1. *Smooth-wall structure*

The mathematical structure of the exchange of leading-order balance in (1.1) across layer III is of central importance. Analysis of (1.1) indicates that this structure is self-similarly replicated on each layer of a continuous hierarchy of scaling layers that increase in width with increasing y (Fife *et al.* 2005, 2009). As noted on figure 2(*b,d*), this layer hierarchy (the so-called L_β hierarchy) extends from $y = O(\nu/u_\tau)$ ($y_{pi}^+ \simeq 7$) to $y = O(\delta)$ ($y_{po}^+ \simeq 0.5\delta^+$). These positions coincide with the inner and outer peaks of the *TI* profile. The mean momentum equation admits an invariant form on the portion of the L_β hierarchy where the leading-order balance is $MI + TI = 0$. On this domain, the distribution of layer widths, W, approaches a linear function of y. This invariant form underlies the existence of a similarity solution that asymptotically coincides with a logarithmic mean velocity profile, e.g. Klewicki (2013*a*). Like all similarity solutions, there is a coordinate stretching function that preserves solution invariance for changing parameter values, e.g. Hansen (1964). In the smooth-wall flow, δ^+ is the only parameter. Here the stretching function is $\phi = \partial y/\partial W$ (Fife similarity parameter), which approaches a constant, $\phi = \phi_c$, on the inertial domain as $\delta^+ \to \infty$.

A number of statistical properties are either predicted by, or empirically correlate with, this similarity structure. One prediction is that the mean vorticity magnitude, $|\Omega_z^+| \simeq \partial U^+/\partial y^+$, decreases with y^+ such that it is $O(1/\sqrt{\delta^+})$ at $y^+ = O(\sqrt{\delta^+})$. Existing smooth-wall boundary layer, pipe and channel flow data support this prediction; for each flow $|\Omega_z^+|\sqrt{\delta^+}$ equals unity at $y^+/\sqrt{\delta^+} \simeq 2.6$, i.e. near the onset of the inertial domain (Klewicki 2013*b*; Vincenti *et al.* 2013). Correlative measures of self-similar behaviour on the $\phi \rightarrow \phi_c$ domain (or those marking its onset) include where the skewness of u, $S(u)$, crosses zero, where the diagnostic plot of Alfredsson *et al.* (2011) (u'/U versus U/U_∞) exhibits its linear dependence, and where the even statistical moments of u exhibit a logarithmically decreasing profile (Marusic *et al.* 2013; Meneveau & Marusic 2013; Vincenti *et al.* 2013; Zhou & Klewicki 2015).

2.2. *Extension to rough-wall flows*

The hypothesized extension to rough-wall flows uses y_m as a surrogate for the inertial domain onset, as described in §1.2. This extension embraces most, if not all, of the accompanying implications. In rough-wall flows the same physical length replaces the purely Reynolds number dependent length, $y_m = O(\sqrt{\nu\delta/u_\tau})$, relevant to smooth-wall flows. MKW13 show that when consistently normalized using u_τ and y_m the mean vorticity profiles from smooth and rough flows merge near y_m. The recent analysis of pipe flow DNS by Saha *et al.* (2015) provides additional corroboration. The geometric simplicity of their sinusoidal roughness allowed the mean pressure gradient in corrugated-wall pipe flow to be expressed as an explicit function of the roughness height. This consequently provided an analytical expression for the length scale characterizing the transition to inertial mean dynamics and an invariant form of the mean momentum equation. As prescribed by the transformations underlying this invariant form, the normalized U and T profiles were shown to respectively adhere to invariant profiles for varying k_s^+ and δ^+.

One part of the present effort is to clarify the extent to which this characteristic length is reflected in the properties of the advective transport mechanism, $\langle v\omega_z \rangle$, underlying the *TI* term *vis-á-vis* (1.4). Another part is to determine if the self-similar behaviours observed on the inertial domain of the smooth-wall flow ($2.6\sqrt{\delta^+} \lesssim y^+ \lesssim 0.5\delta^+$) are also operative on the analogously defined inertial layer for rough-wall flows. Here, it is relevant to note that Castro *et al.* (2013) have shown that the appropriately modified diagnostic function of Alfredsson *et al.* (2011) exhibits linear behaviour in the outer region of rough-wall flows, and that smooth-wall data suggest that the domain of this linear region coincides with, or slightly exceeds, the inertial portion of the layer hierarchy, $2.6\sqrt{\delta^+} \lesssim y^+ \lesssim 0.5\delta^+$ (Klewicki *et al.* 2015; Zhou & Klewicki 2015).

3. Experiments

3.1. *Wind tunnel facility*

The wind tunnel used in the present experiments is the same described by MKW13. As depicted in figure 3, the flow is drawn by a blower located downstream of a 0.61 m × 1.2 m × 8.5 m test section. In order to maintain a nominally zero streamwise pressure gradient, the top wall of the tunnel diverged at an angle of 0.68°. The turbulence management section consisted of a series of screens and honeycomb having the same cross-section as the tunnel test section. This design avoids the possibility of streamwise vorticity generation associated with a contraction,
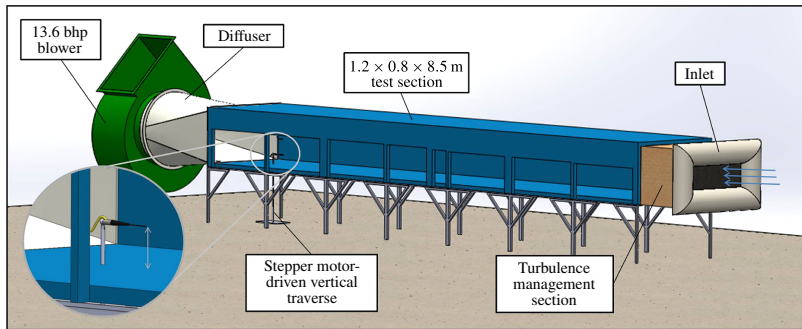
FIGURE 3. (Colour online) Depiction of the UNH 8.5 m boundary-layer tunnel. The hot-wire probe is depicted *in situ* at $x = 8$ m downstream from the tunnel inlet.

but is also best suited for low-speed testing, as in the present study. Hauptman (2010) documented that smooth-wall boundary layers in this tunnel adhered to properties expected of the canonical two-dimensional zero pressure gradient flow. His measurements indicated a streamwise gradient in the static pressure coefficient of less than 0.02. According to Murlis *et al.* (1982), this variation is deemed to be negligible. Preston tube measurements indicate spanwise uniformity in the friction velocity to within $\pm 1\%$ across the central 0.7 m span, while the streamwise freestream turbulence intensity measurements range from 0.3 to 0.37%, depending on the flow speed. Rough-wall boundary-layer measurements from this tunnel are documented in MKW13, as well as herein.

3.2. *Rough surfaces investigated*

Three different rough surfaces were used in the experiments; coarse sandpaper (24 grit), pea-gravel and square bars. These surfaces nominally mimic those used in MKW13. All of the rough surfaces were installed along the entire length of the test section. Smooth-wall profiles were also acquired for comparison. For consistency, the sandpaper and pea-gravel surfaces were installed using 19 mm thick panels of tongue-in-groove particle board. The rough material was glued to the panels, and subsequently installed along the full length of the tunnel. Each panel spanned the entire width of the test section. Any residual gaps at the panel seams were smaller than the height of the roughness. Figure 4 provides images and length scale information pertaining to the sandpaper and pea-gravel surfaces. The bar roughness was created using rigid $d = 12.7$ mm square plastic bars that spanned the width of the tunnel and that were spaced in x at 10 cm intervals, or 8 times the bar height. A notable difference between the present square bar measurements and those of MKW13 is that the present measurements were acquired at $x = 8d$ downstream of the last bar, while the MKW13 measurements were acquired at $x = 4d$ from the last bar.

3.3. *Sensors and instrumentation*

A thermal anemometry sensor was designed and built to acquire the present velocity and vorticity measurements (Ebner 2014). For a properly designed experiment, hot-wire probes have a demonstrated capacity to obtain spatially well-resolved vorticity measurements that also have a frequency resolution suitable for computing
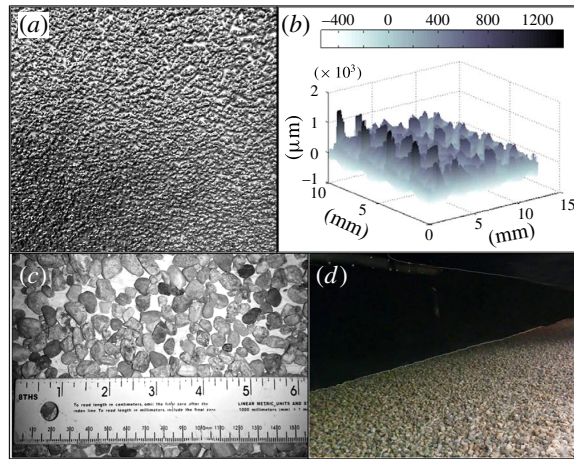
FIGURE 4. (Colour online) (*a*) Image of the 24-grit sandpaper roughness. (*b*) Surface characterization of 24-grit sandpaper roughness (courtesy of M. Schultz) as adapted from Mehdi (2012). (*c*) Image of the pea-gravel surface with a ruler shown for scale. (*b*) Pea-gravel roughness distributed along the 8 m test section.

spectra, e.g. see Tropea *et al.* (2007). For such measurements, the temporal resolution should capture the signature of the high-frequency motions with sufficient fidelity, while the sensor size needs to be small enough to adequately resolve the spatial scales of the pertinent vortical motions. In wall-bounded turbulent flows the smallest motions have a size that is $O(\nu/u_\tau)$ and a characteristic frequency that is $O(u_\tau^2/\nu)$. For the present experiments, the smallest value of ν/u_τ was 21 µm (see table 1). Thus, in these experiments the characteristic dimension of the spanwise vorticity (ω_z) sensor ranged between 10.6 and 23.8 viscous units. Given the primary focus on the inertial domain (nominally beyond y_m), this spatial resolution is deemed sufficient to discern the properties of the motions underlying turbulent momentum transport. Commensurate with the theory described in § 2, the conclusions drawn from the present analyses indicate that the momentum transporting motions have a size comparable to y_m. Thus, an important indication that the present measurements had sufficient spatial resolution is that, at its minimum, y_m exceeded the characteristic sensor dimension by about a factor of 8, see table 1.

The four wire ω_z probe is shown schematically in figure 5. The configuration of an ×-array of wires nested within a parallel array was originally developed and used by Foss & Haw (1990), also see Rajagopalan & Antonia (1993) and Priyadarshana *et al.* (2007). The present probe derives from a number of advances in the manufacturing process (Ebner 2014). These allow its repeatable construction at half the characteristic size of the original 1.0 mm sensor. The sensor design co-locates the measurements from the two arrays. This is accomplished by weaving the ×-array through the parallel array. The presence of silver plating on the outer third of each wire makes this feasible, since the plated portion is not sensitive to velocity fluctuations. The net result is a 0.5 mm × 0.5 mm frontal area measurement domain over which wire interference (wake) effects are negligible. The wires on the sensor come as 30 µm diameter silver coated platinum 10 % rhodium (Pt10 %Rh). After they are soldered to the prongs, nitric acid is used to remove the silver plating over the central 0.5 mm region of each wire. The unplated Pt10 %Rh wire has a 2.5 µm diameter.
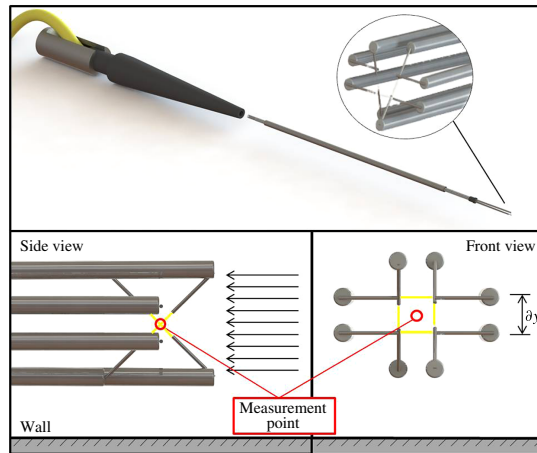
FIGURE 5. (Colour online) Four wire Foss-style ω_z sensor used to acquire the present measurements. Note that both the unplated wire length (2.5 μm diameter) and the wire spacings are $\Delta y = \Delta z = 0.5$ mm.

Surface	U_∞ (m s^{-1})	u_τ (m s^{-1})	ν/u_τ (m × 10^{-5})	δ_{99} (m)	H	δ^+	k_s^+	y_m^+	ℓ^+	ΔU^+	f_c^+	TU_∞/δ
Smooth	8.05	0.316	4.7	0.100	1.29	2 102	n/a	82	10.6	n/a	0.45	19 300
Sandpaper	9.21	0.470	3.2	0.123	1.38	3 832	71.5	174	15.6	6.9	0.34	18 000
Pea-gravel	9.21	0.540	2.9	0.206	1.47	7 173	435	313	17.2	11.3	0.35	10 700
2-D bars	9.41	0.742	2.1	0.310	1.50	15 064	4376	618	23.8	17	n/a	7 300

TABLE 1. Summary of the experiment specifications and flow parameters. H refers to the shape factor, ratio of displacement to momentum thickness, k_s^+ is the inner-normalized equivalent sand grain roughness, $\ell = 0.5$ mm is the wire length, which also equals the wire spacings in the ×- and parallel arrays, and T is the sampling duration.

The sensor was operated using AA Labs AN1003 constant temperature bridges at a heating ratio of 1.2 (i.e. at about 200 K above ambient). An impulse test of the probe–circuitry system indicated a frequency response in excess of 20 kHz, while the estimated maximum frequency encountered in the flows investigated was approximately 13.5 kHz. The sensor was mounted in the wind tunnel test section and calibrated *in situ* using a custom built articulating jet facility (Ebner 2014). Calibrations were performed before and after each experiment, and the experiment was repeated if the discrepancies between any wire's pre- and post-calibration was greater than about 2 %. A King's law calibration equation was used for the parallel-array wires. The ×-array calibration involved surface fits of data acquired over a series of discrete velocity magnitudes (typically 6–8) spanning the flow speed range encountered in the given experiment, and flow angles ranging between ±40°. The calibration velocities were determined using pressure measurements (MKS Baratron 698A 10 Torr transducer, ±0.12 % full scale accuracy), while the motor controller on the facility set jet angles at $0.018 \pm 0.0009°$ increments.

The individual velocity gradient contributions to the fluctuating spanwise vorticity, $\omega_z = \partial v/\partial x - \partial u/\partial y$, were calculated at each instant. The $\partial u/\partial y$ gradient was estimated

by first-order finite differencing the parallel array u velocities, $\partial u/\partial y \simeq \Delta u/\Delta y$. The $\partial v/\partial x$ gradient was estimated from the $v(t)$ time series and Taylor's hypothesis. Here a sliding second-order curve was fit to the $v(t)$ data over an advected length, Δx, that was selected to nominally equal Δy. This fit was then differentiated, and the local mean velocity U was used to convert the time derivative to a spatial derivative. Signal attenuation was present due to the finite length of the individual wires and the wire spacings. Resolution effects associated with the wire lengths ($11 \lesssim \ell^+ \lesssim 24$) are expected to be less than 5 % on the inertial domain of interest (Hutchins *et al.* 2009). Attenuation associated with the wire spacing ($11 \lesssim \Delta y^+ \lesssim 24$) is more significant. Based on DNS and experimental studies, this attenuation is estimated to be no more than 15 % on the domain of interest (Klewicki & Falco 1990; Antonia *et al.* 1993).

The experimental data were acquired at 30 kHz using a Data Translation 9836 16-bit simultaneous sample-and-hold analogue to digital converter. All but the square bar data were analogue filtered at inner-normalized cutoff frequencies between $f_c^+ = 0.35$ and 0.45, see table 1. These values nominally conform to the criteria recommended by Hutchins *et al.* (2009) for velocity fluctuations. As such, they are likely to have a small filtering effect on the high end of the ω_z spectrum. The f_c^+ values are close to the effective cutoff of the unfiltered data from the square bar experiment. Each time series was sampled over 240 s. At a minimum, this corresponds to about 7300 integral time scales, δ/U_∞. According to Klewicki & Falco (1990), a sampling duration of approximately $6000\delta/U_\infty$ is sufficient to ensure a better than ± 5 % statistical convergence for the skewness of u, v, and ω_z, with significantly smaller convergence uncertainty for either the variance or kurtosis. Ebner (2014) estimates that the uncertainties in the instantaneous u, v and uv measurements are ± 1.5 %, ± 7.5 % and ± 7.6 %, respectively. Based upon the previous analysis of MKW13, the present u_τ values (see below) are estimated to have an uncertainty of ± 4 %.

3.4. *Experiment procedures*

The position of the sensor relative to the sandpaper and pea-gravel roughness was determined using the method of MKW13. Here a precision machined steel block of known thickness was laid on top of the roughness, and the centre of the probe was aligned with the wall-normal position of the block's upper surface. This located the probe relative to the crest plane of the given roughness. The probe was then traversed much closer to the rough surface, and the given profile was acquired. The virtual origin of the sandpaper and pea-gravel roughness was subsequently estimated using the mean velocity data. Following convention, this involves assuming the existence of a region of logarithmically varying U/U_∞ for a range of yU_∞/ν, e.g. Connelly, Schultz & Flack (2006). This procedure used a value of 0.41 for the von Kármán constant. For the sandpaper and pea-gravel roughness the resulting shifts in origin were 0.4 mm and 4.8 mm, respectively. In the square bar experiments the origin was taken to be the smooth wall.

4. Flow parameters and data analysis methods

Table 1 provides values for a number of relevant parameters. As indicated, the freestream velocity did not vary significantly between the different flows. Note also that for the 2-D bar roughness the estimated boundary-layer thickness, δ_{99}, slightly exceeds the test section half-height. Measurements extending into the freestream,

however, verified the existence of a potential core region. This core exists because the boundary layer on the smooth upper wall of the test section had a much smaller thickness.

The friction velocity estimates in table 1 were found using the method of Mehdi & White (2011). This method was developed for use with experimental data from flows that have stresses that cause surface drag via mechanisms other than viscous shear alone. The formulation develops an expression for the skin friction coefficient in terms of the net wallward flux of streamwise momentum per unit area. Following the approach of Fukagata *et al.* (2002), (1.1) is thrice integrated and the streamwise gradient term is replaced with the mathematically equivalent wall-normal derivative of the total stress, τ_t. The resulting expression for the skin friction is

$$C_f = 4 \int_0^1 (1 - \eta) \tau_t \, \mathrm{d}\eta + 2 \int_0^1 (1 - \eta)^2 \left(-\frac{\partial \tau_t}{\partial \eta} \right) \mathrm{d}\eta, \qquad (4.1)$$

where $\eta = y/\delta$, and τ_t $(= \mu \partial U/\partial y - \rho \langle uv \rangle)$ is normalized using ρ and U_∞. In order to compute the total stress derivative, a Whittaker smoother is applied to the total stress weighted by $(1 - \eta)$, and the derivative of the smoothed profile is then used to compute the skin friction coefficient. A linear fit is used to estimate the values from the peak in the total stress curve to the wall. Further details are given in Mehdi & White (2011).

The value of the inner-normalized equivalent sand grain roughness, k_s^+, is directly related to the downward shift in the mean velocity, ΔU^+. The k_s^+ and ΔU^+ values indicated table 1 are related by the empirical equations of Ligrani & Moffat (1986). Following Ligrani & Moffat (1986) and Jiménez (2004), these relations employed $k_s^+ \leqslant 5$ to specify aerodynamically smooth flow, $5 < k_s^+ \leqslant 70$ to specify transitionally rough flow, and $k_s^+ > 70$ to indicate fully rough flow.

The y_m values for the present rough-wall flows were estimated using (1.2), while $y_m = 1.8\sqrt{\nu\delta/u_\tau}$ was used for the smooth-wall estimate. In connection with this, a re-examination of the MKW13 data reveals that the y_m values for the pea-gravel flow are best estimated using the $y_m/k_s \approx 1$ equation, rather than the $y_m/k_s < 1$ equation, as suggested in MKW13. An issue here is that in laboratory facilities it is difficult to unambiguously attain the $y_m/k_s < 1$ condition, while simultaneously maintaining $\delta \gg k_s$. The estimated value for y_m/k_s in the present pea-gravel flow ranges from approximately 0.42 to 0.72, depending on whether the $y_m/k_s < 1$ or $y_m/k_s \approx 1$ equation in (1.2) is used. Thus, this flow approximately resides between these two regimes.

Part of the present analysis quantifies the streamwise length scales characteristic of the motions of interest, as well as the scales over which these motions interact. One method estimated the wavelength of the peak in the premultiplied spectrum. In this case, an ensemble averaged frequency spectrum was computed using a discrete Fourier transform. The premultiplied wavelength spectrum was then constructed using the local mean velocity and Taylor's hypothesis. For the v and ω_z spectra of primary interest, there was a clear single peak. The wavelength spectra were then smoothed by a Savitzky–Golay filter. A peak region was then easily identified, and a second-order polynomial was fit to this region. The derivative of the curve fit subsequently located the associated peak wavelength, e.g. λ_v.

A measure of the streamwise interaction length between v and ω_z was also found. This involved analysis of the time-delayed correlation curves of $\langle v(t)\omega_z(t \pm \Delta t)\rangle$. As in the studies of Monty *et al.* (2011*b*) and Morrill-Winter & Klewicki (2013), a characteristic time scale was subjectively yet consistently defined at each wall-normal

location as the time duration over which the correlation profile magnitude exceeded 30 % of its maximum measured magnitude. This duration was then converted to an advected streamwise length, l_x, via Taylor's hypothesis using the local mean velocity.

5. Results

This section first presents statistics of u, v and ω_z. Here the analysis largely focuses on the location of the inertial domain and the scaling behaviours of statistics on this domain. This is followed by an investigation of characteristic length scales associated with the $\langle v\omega_z \rangle$ contribution to the *TI* term in (1.1).

5.1. *Velocity statistics*

5.1.1. *Mean, variances and Reynolds shear stress profiles*

The inner-normalized mean profiles of figure 6(*a*) exhibit the characteristic downward shift associated with roughness-induced drag and increasing k_s^+, see table 1. The present mean profiles exhibit good consistency with those of MKW13, except near the wall in the bar roughness flow. This difference is attributable to the aforementioned difference in the measurement location; the near-wall flow in the present hot-wire measurements had twice the streamwise distance to recover from the separated flow downstream of the last bar. Both near the wall and across the logarithmic region, the smooth-wall profile exhibits very good agreement with the DNS of Schlatter & Orlu (2010) and the data from the experiments of DeGraaff & Eaton (2000), but evidences a slightly weaker wake strength than expected. With the addition of the corresponding ΔU^+ values indicated in table 1, the logarithmic portion of the profiles of figure 6(*a*) have been verified to convincingly merge.

Inner-normalized streamwise velocity variance profiles are plotted versus y/δ in figure 6(*b*). For *y*-position consistency with the v and ω_z measurements, the profiles in figure 6(*a,b*) come from the ×-array of the sensor. The results from the individual parallel-array wires have been verified to graphically exhibit the same results ($\pm 2\,\%$), except for the near-wall flow over the bar roughness. While still small, the differences here become more noticeable. Although the data of figure 6(*b*) exhibit some scatter, from these it seems reasonable to conclude that outer similarity is approximately satisfied for the smooth, sandpaper and pea-gravel surfaces. This includes very good agreement with the present smooth-wall data, as well as the smooth-wall profile of DeGraaff & Eaton (2000). Noticeable differences between the present results and those of MKW13 are, however, apparent. The most obvious is associated with the $\delta^+ = 13\,677$ square bar flow. It is rational to suspect this deviation is at least partially attributable to the relative measurement locations between present and MKW13 experiments, and these variations would seem to indicate a breakdown of outer-layer similarity. The other difference is that the sandpaper and pea-gravel profiles of MKW13 are slightly above the present in the region $0.5 \lesssim y/\delta \lesssim 1.0$. This behaviour was also observed by MKW13 in comparisons with measurements by other researchers. The reason for this difference is not known, but the very small characteristic dimension of the MKW13 LDV measurement volume (1–3.5 viscous units) may be a relevant factor.

Profiles of the inner-normalized wall-normal velocity variance are plotted versus y/δ in figure 7(*a*). Generally in accord with previous rough wall $\langle v^2 \rangle^+$ data, the present peak values increasingly exceed unity with increasing δ^+, and thus exhibit increased profile-to-profile variation near their peak values. Even given the scatter, violations of outer similarity seem apparent in the peak region for both the present
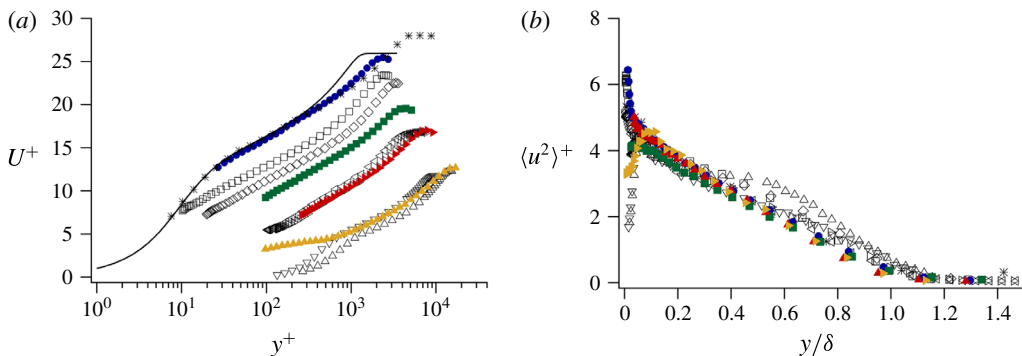
FIGURE 6. (Colour online) Profiles of streamwise velocity statistics; (*a*) inner-normalized mean velocity profile, smooth-wall (●) (blue); sandpaper (■) (green); pea-gravel (▶) (red); square bars (▲) (maize), colour online. Solid line is from the DNS of Schlatter & Orlu (2010) at $\delta^+ \simeq 1250$; smooth-wall profile of DeGraaff & Eaton (2000), $\delta^+ = 4580$ (∗); (*b*) profiles of inner-normalized streamwise velocity variance versus y/δ. Smooth-wall profile of DeGraaff & Eaton (2000), $\delta^+ = 4580$ (∗). Profiles of Mehdi *et al.* (2013) $\delta^+ = 2119$, $k_s^+ = 23$ (□); $\delta^+ = 2915$, $k_s^+ = 39$ (◇); $\delta^+ = 3969$, $k_s^+ = 382$ (◁); $\delta^+ = 5279$, $k_s^+ = 488$ (▷); $\delta^+ = 8733$, $k_s^+ = 3944$ (▽); $\delta^+ = 13\,677$, $k_s^+ = 6451$ (△).
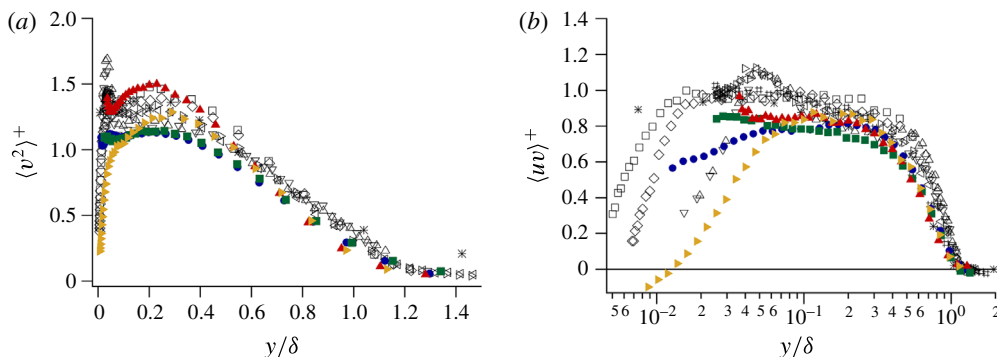
FIGURE 7. (Colour online) (*a*) Inner-normalized wall-normal velocity variance profiles plotted versus y/δ; (*b*) inner-normalized Reynolds shear stress profiles plotted versus y/δ. Smooth-wall profile of DeGraaff & Eaton (2000), $\delta^+ = 4580$ (∗); $\delta^+ = 2915$, $k_s^+ = 56$ profile of Connelly *et al.* (2006) (#); other symbols same as in figure 6.

pea-gravel and square bar flows, while the sandpaper and smooth-wall profiles exhibit much closer agreement. The apparent violation of outer similarity in the peak region by the present and MKW13 data is more pronounced than other observations, e.g. Flack *et al.* (2005).

Although the present $-\langle uv \rangle^+$ profiles of figure 7(*b*) exhibit good self-consistency, over most of the outer region they are also of noticeably smaller magnitude than the MKW13 profiles. These $-\langle uv \rangle^+$ profiles do, however, exhibit close agreement with the smooth-wall profile of DeGraaff & Eaton (2000) and the rough-wall profile of Connelly *et al.* (2006) shown in figure 7(*b*). Generally consistent with asymptotic
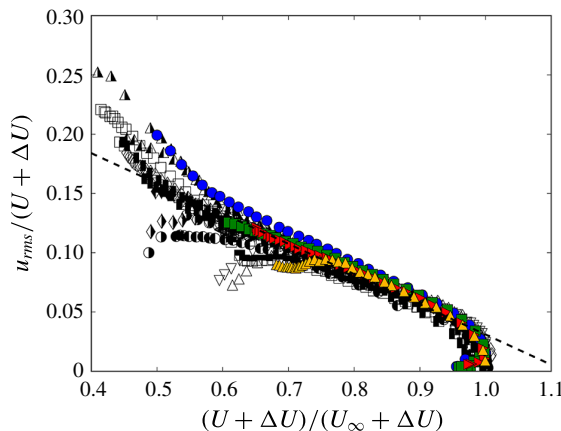
FIGURE 8. (Colour online) Version of the diagnostic plot of Alfredsson *et al.* (2011) adapted for rough-wall flows (Castro *et al.* 2013). Profiles of Krogstad & Antonia (1999): left-filled ○, $\delta^+ = 5224$, $k_s^+ = 344$; right-filled ○, $\delta^+ = 1987$, $k_s^+ = 258$. Profiles of Connelly *et al.* (2006): left-filled □, $\delta^+ = 2915$, $k_s^+ = 56$; right-filled □, $\delta^+ = 3022$, $k_s^+ = 36$; top-filled □, $\delta^+ = 5997$, $k_s^+ = 1150$. Profiles of Brzek *et al.* (2007): left-filled △, $\delta^+ = 767$, $k_s^+ = 34$; right-filled △, $\delta^+ = 1175$, $k_s^+ = 16$; left-filled ◊, $\delta^+ = 1555$, $k_s^+ = 92$; right-filled ◊, $\delta^+ = 3355$, $k_s^+ = 228$. Present symbols same as in figure 6.

behaviour, with increasing Reynolds number there is plateau region around the $-\langle uv \rangle^+$ peak, and the measured peak values tend to migrate toward unity with increasing Reynolds number.

5.1.2. *Diagnostic plot*

Recent analyses by Zhou & Klewicki (2015) suggest that for smooth-wall flows the bounds of the linear region of the diagnostic plot of Alfredsson *et al.* (2011) nominally match, or slightly exceed, the estimated bounds of the inertial domain, $2.6\sqrt{\delta^+} \lesssim y^+ \lesssim 0.5\delta^+$. The rough-wall version of the diagnostic plot (figure 8) is modified to account for the downward mean profile shift indicated in figure 6(*a*) Castro *et al.* (2013). If the approximately linear region universally corresponds to the inertial domain, then under the present hypothesized extension for rough-wall flows, its starting position, y_s, should be located at $O(y_m)$ and its ending position, y_e, at $O(\delta)$ – presumably near $y/\delta = 0.5$ as in the smooth-wall case.

Figure 8 shows the modified diagnostic plot for the present data, the data of MKW13, and the other researchers' data used in the study of Mehdi *et al.* (2010). All of the profiles on this plot exhibit an outer region of approximately linear dependence. The apparent variations in the slope are likely to be at least partially attributable to experimental uncertainties, or the differences from one facility to the next. The extent of the linear region was estimated herein by an arguably more robust method than used by Zhou & Klewicki (2015). This involves taking second derivatives of the profiles and identifying the zone where this derivative is zero. Since the data contain noise, they were first interpolated to a finer grid and smoothed via convolution with a double differentiated Gaussian kernel. The result is a function that has (nominally) zero value where the diagnostic curve is linear. Near the start of the region of interest the smoothed derivative consistently exhibited a maximum,
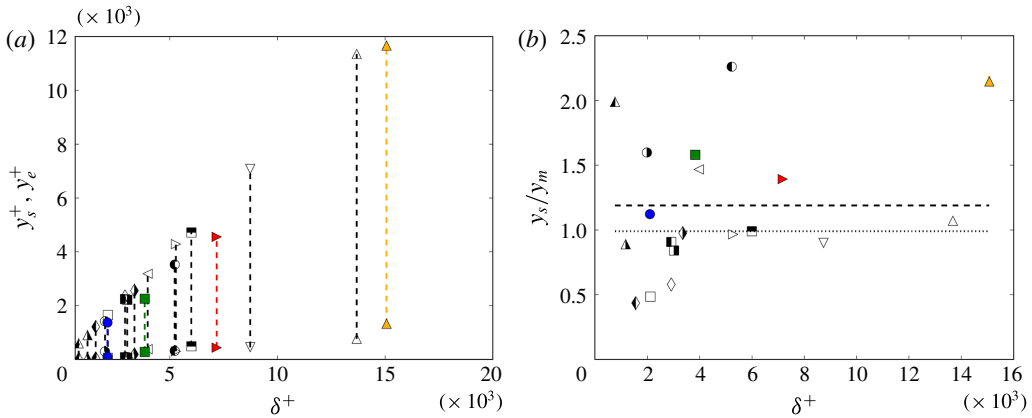
FIGURE 9. (Colour online) Characteristics of the diagnostic plot; (*a*) estimated inner-normalized start (y_s^+) and end (y_e^+) positions of the linear region plotted versus δ^+; (*b*) y_s/y_m versus δ^+. Dashed and dotted horizontal lines respectively represent the mean and median of the data ensemble. Symbols same as figure 8.

while beyond the end it consistently exhibited an identifiable minimum. The positions of these maxima were used to estimate y_s and y_e, with the results plotted versus δ^+ in figure 9(*a*). The y_e^+ data convincingly suggest a linear dependence on δ^+, with a slope of about 0.75. On the other hand, the y_s^+ data suggest a dependence that is intermediate to inner or outer scaling. The y_s/y_m data in figure 9(*b*) exhibits considerable scatter, with y_s/y_m ranging from near 0.5 to about 2.5. The present data vary between $1.1 \lesssim y_s/y_m \lesssim 2.1$. Despite this scatter, the results of figure 9(*b*) suggest that $y_s = O(y_m)$ for varying k_s^+ and δ^+.

5.1.3. *Skewness and kurtosis profiles*

The skewness is a measure of the asymmetry of a probability distribution about its mean. In recent years, the skewness of the u fluctuations, $S(u)$, has received attention owing to its connection to the correlation coefficient, R, that describes the modulation of the near-wall flow by the inertial motions farther from the wall (Mathis *et al.* 2011; Duvvuri & McKeon 2015). Physically, the position of the zero crossing, y_{zc}, of either R or $S(u)$ is thought to nominally coincide with the average position of the inertial (superstructure) motions closest to the wall. Accordingly, this position is expected to coincide with where the leading-order mean force balance transitions to $MI = TI$, regardless of whether the flow is over a smooth or rough surface. Consistent with this, Vincenti *et al.* (2013) provide evidence that $y_{zc}^+ \simeq 2.6\sqrt{\delta^+}$ for smooth-wall flows up to $\delta^+ \simeq 20\,000$. The rough-wall extension of the theory (described in §2) calls for this position to nominally scale with y_m.

Figure 10(*a*) shows $S(u)$ profiles versus y^+ for the present flows as well as those from MKW13. Under inner-normalized distance from the wall, the profile-to-profile variations are significant, with y_{zc} exhibiting clear increases with increasing δ^+ and k_s^+. Figure 10(*b*) plots $S(u)$ versus y/y_m, and this normalization is seen to effectively organize the data starting near $y/y_m = 2$. Here it is useful to point out that, relative to the sources of uncertainty discussed in §3, the effects of spatial resolution are expected to be negligible on the inertial domain, and that statistical convergence is less than $\pm 5\,\%$ for the third moments and less than $\pm 3\,\%$ for the fourth moments. Note
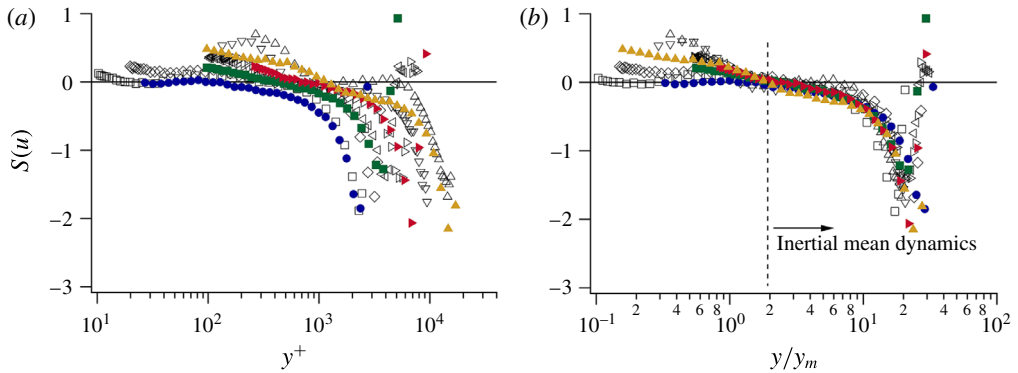
FIGURE 10. (Colour online) Profiles of the streamwise velocity skewness, $S(u)$; (*a*) versus y^+; (*b*) versus y/y_m. Symbols same as in figure 6.

Surface	y_m^+	y_{zc}/y_m	y_1/y_m
Smooth	82	1.37	2.62
Sandpaper	174	2.30	2.45
Pea-gravel	313	2.32	2.58
2-D bars	618	1.89	2.11

TABLE 2. Properties correlated with the starting location of the self-similar inertial region. Position where $S(u)$ crosses zero in figure 10 is denoted by y_{zc}. Position where $|\Omega_z|y_m/u_\tau$, passes through unity in figure 13 is denoted by y_1.

that the square bar roughness profiles apparently have a different shape than the others interior to $y/y_m \simeq 2$ (not surprisingly), and retain noticeably different shapes beyond $y/y_m \simeq 2$. This latter feature is consistent with a significant violation of outer similarity. Also, while the overall scale separation (as reflected by δ^+) varies significantly in these flows, the profiles of figure 10(*b*) demonstrate that the present experiments only cover relatively small changes in the scale separation reflected by δ/y_m. The zero crossing for each profile from the present experiments was estimated using a logarithmic curve fit of the $S(u)$ data over the region of interest. The resulting y_{zc} data are presented in table 2. The present smooth wall $S(u)$ profile crosses zero at $y^+ \simeq 2.47\sqrt{\delta^+} = 1.37y_m^+$. For the rough-wall flows, y_{zc} is expected to scale like y_m, to within an $O(1)$ coefficient. The results listed in table 2 are consistent with this.

The $S(v)$ profiles of figure 11 exhibit results similar to the $S(u)$ data in figure 10. Beginning near the onset of the inertial region ($y/y_m \simeq 2$) the $S(v)$ profiles of figure 11(*b*) display small positive values over a range of wall-normal locations. Similar, but less dramatic, behaviours are also observed for the kurtosis profiles of u and v shown in figure 12(*a,b*), respectively. The smooth- and rough-wall profiles of $K(u)$ and $K(v)$ display remarkable consistency on the inertial domain, with each $K(u)$ profile exhibiting slightly sub-Gaussian (<3) values, and each $K(v)$ profile exhibiting slightly super-Gaussian (>3) values. Examination of these profiles versus y/δ (not shown) reveals that these sub- and super-Gaussian domains nominally extend to $y/\delta \simeq 0.5$. This location coincides with the estimate for, y_{po}, the upper bound of the self-similar layer hierarchy (figure 2).
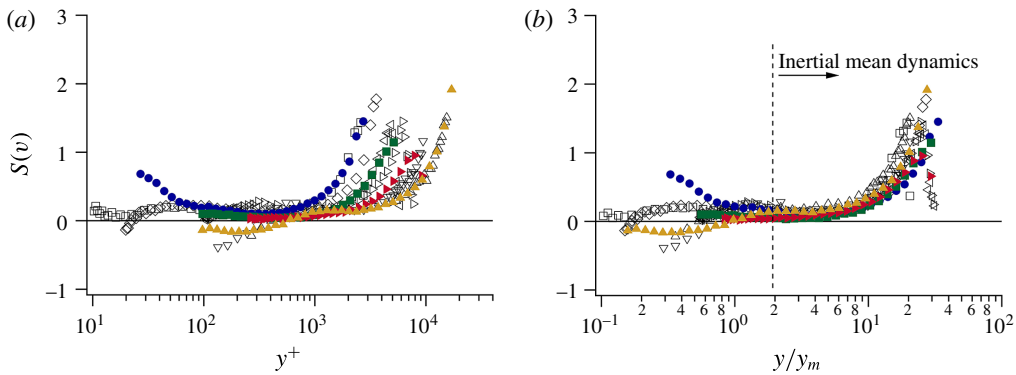
FIGURE 11. (Colour online) Profiles of the wall-normal velocity skewness, $S(v)$; (*a*) versus y^+; (*b*) versus y/y_m. Symbols same as in figure 6.
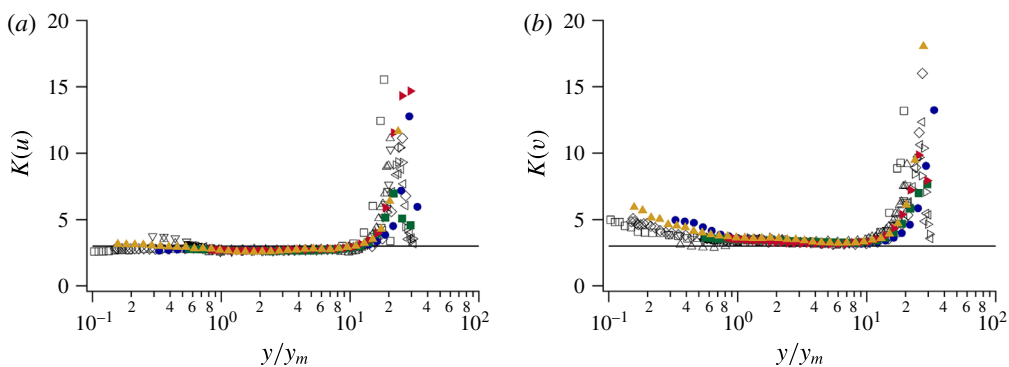

FIGURE 12. (Colour online) Kurtosis profiles of u and v versus y/y_m. (*a*) Streamwise velocity; (*b*) wall-normal velocity. Symbols same as in figure 6.

5.2. *Spanwise vorticity statistics*

5.2.1. *Mean and variance profiles*

Profiles of the inner-normalized mean vorticity magnitude, $|\Omega_z^+| \simeq \partial U^+/\partial y^+$, are presented in figure 13(*a*). Consistent with the mean velocity profile data of figure 6(*a*), to within the measurement uncertainty each of these profiles exhibits a region of power-law decay with slope close to -1. The y^+ range and $|\Omega_z^+|$ values over which this power-law dependence exists, however, varies considerably depending upon the surface condition. The rough-wall extension of the present theory postulates that this starting position is a function of both roughness and Reynolds number (Mehdi *et al.* 2013; Saha *et al.* 2015). Accordingly, the theory prescribes that the mean vorticity profiles can be brought into alignment beginning near the onset of the inertial domain by scaling the data as in figure 13(*b*). Here the start of the inertial domain is nominally aligned by normalizing the wall-normal position with y_m. Similarly, the mean vorticity magnitude is rendered $O(1)$ where $y/y_m = O(1)$ via normalization by u_τ/y_m. For smooth-wall flow, these scaling behaviours follow directly from the differential transformations required to produce an invariant form of (1.1) (Klewicki 2013*b*). The smooth-wall data of figure 13(*b*) exemplify these behaviours. Consistent with the results of MKW13, the profiles of figure 13(*b*) merge on an interior domain
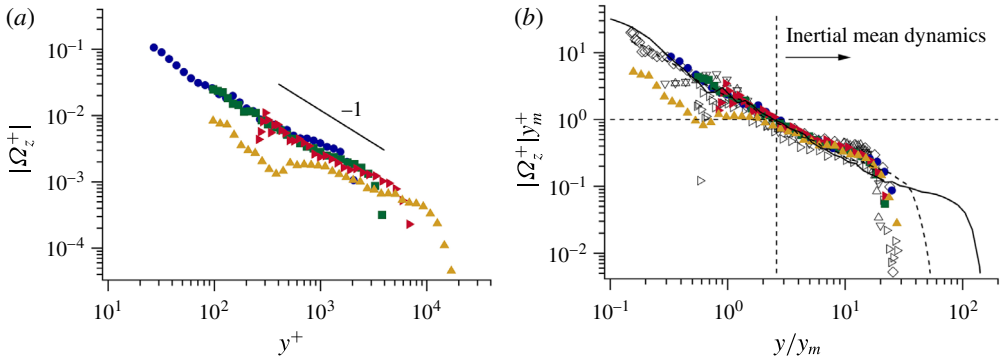
FIGURE 13. (Colour online) Normalized profiles of the mean vorticity magnitude, $|\Omega_z| \simeq \partial U/\partial y$; (a) inner-normalized versus y^+, (b) normalized using y_m and u_τ and plotted versus y/y_m; Hutchins *et al.* (2009) $\delta^+ = 16\,700$, smooth (——); Schultz & Flack (2007) $\delta^+ = 4760$, smooth (- - -); other symbols same as in figure 6. Vertical dashed line at $y/y_m \simeq 2.5$.

beginning where the stretched coordinate, y/y_m, is $O(1)$. The positions, y_1/y_m, where $|\Omega_z|y_m/u_\tau = 1$ are given in table 2. The square bar roughness data of figure 13 only approximates the other profiles in a small region beyond the onset the inertial domain, $y/y_m \gtrsim 2$. Clearer indications of a deviation from self-similar structure for this flow are given by the ω_z statistics described below.

A number of normalized forms of the spanwise vorticity variance profile were examined. None except those in figures 14 and 15 provided evidence of (approximate) invariance on the inertial domain. The inner-normalized profiles of figure 14(a) exhibit behaviours similar to the $|\Omega_z|^+$ profiles of figure 13(a); each profile displays a nearly constant negative slope over a y^+ domain, but the beginning and end points of these domains do not coincide. Similar to the $|\Omega_z|^+$ profiles, this situation is apparently rectified in figure 14(b) by plotting $\langle \omega_z^2 \rangle^+ y_m^+$ versus y/y_m. Note that when expressed in terms of a quantity having the dimensions of Ω_z (i.e. the r.m.s., $\omega_z' = \sqrt{\langle \omega_z^2 \rangle}$) the scaling of figure 14(b) is seen to be a mixture of inner and intermediate normalizations: $\langle \omega_z^2 \rangle^+ y_m^+ = (\omega_z' \nu/u_\tau^2)(\omega_z' y_m/u_\tau)$.

As described by Morrill-Winter & Klewicki (2013), an appropriate 'outer' normalization involves shifting the origin to the onset of the inertial domain, and normalizing the variations from this position by the width of layer IV. To within the approximation that y_m is a surrogate for the beginning of the inertial domain, this entails using the coordinate, $(y - y_m)/(\delta - y_m)$. Figure 15 shows the present data under this normalization. For a range of $(y - y_m)/(\delta - y_m)$ beginning near the origin, the non-square bar profiles show very good agreement; albeit the pea-gravel data shows an apparent deviation to slightly smaller values. This is consistent with a diminished spatial resolution relative to the smooth wall or sandpaper roughness flows.

The square bar roughness profiles in figures 13–15 noticeably depart from the others. Klewicki (2013b) used DNS channel data of $\omega_z'/|\Omega_z|$ to evidence that the mean and r.m.s. spanwise vorticity are self-similarly related starting very near the wall and extending to increasing y^+ locations with increasing δ^+. This behaviour is apparently consistent with classical law of the wall scaling arguments. The results of figure 16(a) reinforce this finding (for the smooth, sandpaper and pea-gravel surfaces), under the proviso that the self-similar behaviour on the inertial domain
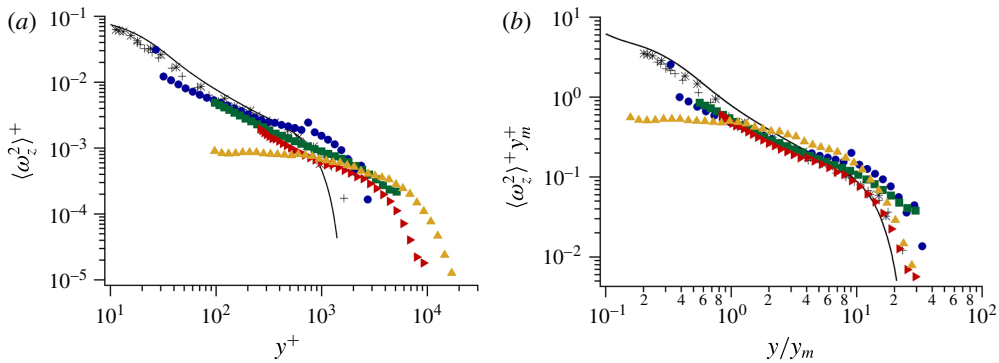
FIGURE 14. (Colour online) Normalized profiles of the spanwise vorticity variance; (*a*) inner-normalized versus y^+, (*b*) normalized using y_m and u_τ and plotted versus y/y_m. Smooth-wall profiles of Klewicki & Falco (1990), $\delta^+ \simeq 970$ (∗); $\delta^+ \simeq 1500$ (+). Other symbols same as in figure 6.
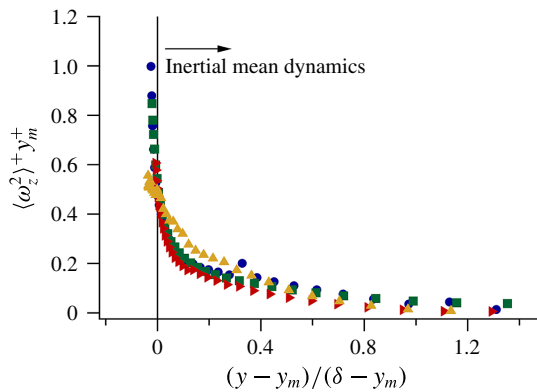

FIGURE 15. (Colour online) Layer IV normalization of the present vorticity variances. Symbols same as in figure 6.

is shifted from flow to flow according to the combined influences of roughness and Reynolds number. The results of figure 16(*a*) also indicate that, relative to the mean, there is an excess of vorticity variance in the square bar flow. Assuming the normalizations of figures 13(*b*) and 14(*b*) produce invariant profiles, alignment of the inertial domain is realized by forming the ratio of the inner-normalized spanwise vorticity variance to its inner-normalized mean. The profile of this ratio is shown in figure 16(*b*). (Note that $\langle \omega_z^2 \rangle^+ / |\Omega_z|^+ = \omega_z'^+ \omega_z' / |\Omega_z|$.) Even with the considerable data scatter, it is apparent that three of the profiles are in nominal agreement on the inertial domain. The data from square bar flow are, however, clearly distinct.

5.2.2. *Skewness and kurtosis profiles*

In §1.3 it was noted that outer-layer similarity is likely to hold when the vorticity stretching and three-dimensionalization processes on layer II are such that the uniform momentum zone/vortical fissure structure can, to a good approximation, form on layer IV. The present $\langle \omega_z^2 \rangle$ data suggest nominal outer-layer similarity for the smooth,
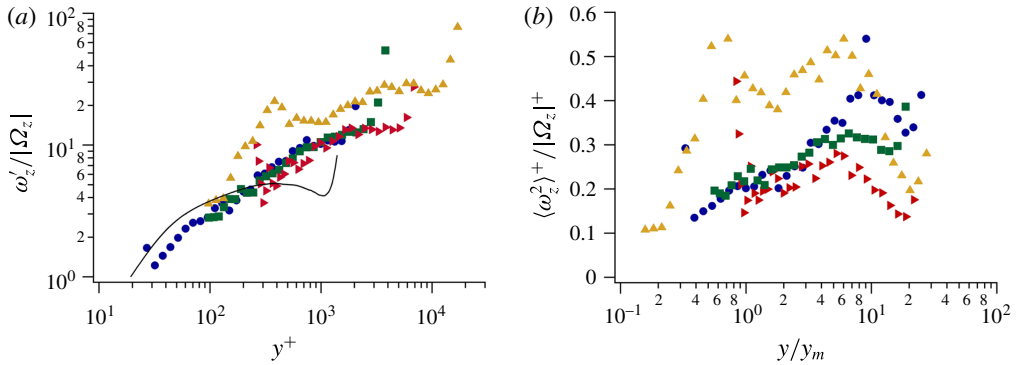
FIGURE 16. (Colour online) Ratio of (*a*) the r.m.s. spanwise vorticity to the mean vorticity versus y^+, (*b*) the inner-normalized variance of ω_z to the inner-normalized mean vorticity versus y/y_m. Symbols same as in figure 6.
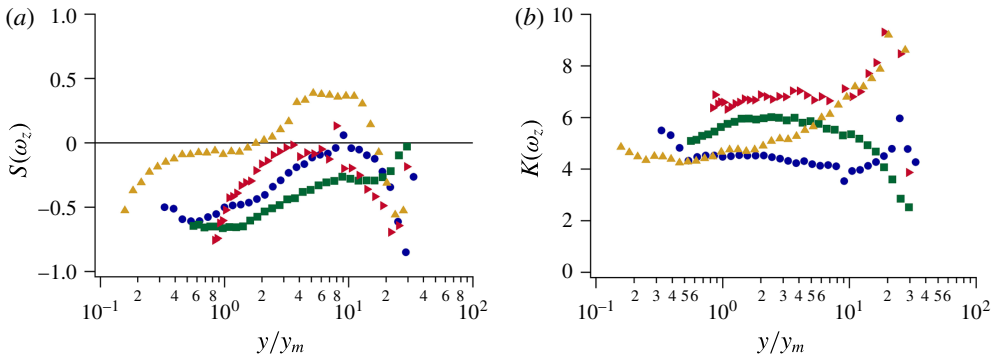

FIGURE 17. (Colour online) Higher-order central moment profiles of the spanwise vorticity fluctuations; (*a*) skewness, (*b*) kurtosis. Symbols same as in figure 6.

sandpaper and pea-gravel flows. Hong *et al.* (2011) found that roughness can leave its signature on the vortical motions, not only near the roughness, but throughout the flow. From this, MKW13 speculated that outer similarity is at best an approximation, since features of outer region vortical motions are likely to retain connection to the roughness-induced three-dimensionalization processes that led to their initial formation. The ω_z skewness and kurtosis profiles of figure 17 support this proposal to the extent that these higher-order moment profiles for the smooth, sandpaper and pea-gravel flows exhibit clear differences. In this regard, while the effects of spatial resolution on the present ω_z measurements are non-negligible on the inertial domain, the profile-to-profile variations in figure 17(*a,b*) greatly exceed the anticipated influence of such effects, as well as those associated with statistical convergence, see § 3. In particular, the qualitatively distinct sign change (to positive values) of the $S(\omega_z)$ profile from the square bar flow evidences an especially telling deviation from the self-similar behaviours that are more reasonably approximated by other flows. Lastly, one apparently common feature is the rapid rise in each $S(\omega_z)$ profile starting near the onset of the inertial domain ($y/y_m \simeq 2$).
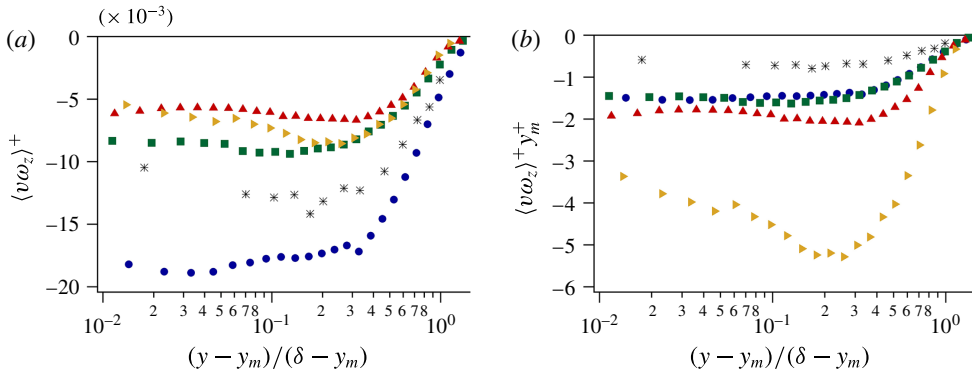
FIGURE 18. (Colour online) Inertial layer profiles of the correlation between v and ω_z; (*a*) normalized by u_τ^3/ν, (*b*) normalized by u_τ^2/y_m. Symbols same as in figure 14.

5.3. $v\omega_z$ *correlation analysis*

Of the terms appearing in (1.4), the $\langle v\omega_z \rangle$ correlation is the most significant on the inertial domain. This section examines properties associated with this correlation, and specifically the length scale over which v and ω_z correlate.

5.3.1. *Single-point correlation structure*

Profiles of the $\langle v\omega_z \rangle$ correlation are examined under two normalizations. Figure 18(*a*) reveals that for $y_m \lesssim y \lesssim 0.5\delta$ each of the $\langle v\omega_z \rangle^+$ profiles exhibit distinct but nominally constant values, and for greater y diminish toward zero as $y \to \delta$. No trend with Reynolds number or roughness is evident under this normalization. Based upon the apparent success of the ω_z variance normalization of figure 15(*b*), figure 18(*b*) considers a normalization of $\langle v\omega_z \rangle$ that incorporates y_m. (Note that $\langle v\omega_z \rangle^+ y_m^+ = \langle v\omega_z \rangle y_m/u_\tau^2$.) Here the profiles for the smooth wall and sandpaper surfaces convincingly merge, while the pea-gravel profile exhibits relatively good agreement. The bar roughness profile is, however, clearly distinct. The profiles of figure 18(*b*) exhibit increasing magnitude with increasing roughness and Reynolds number.

While the inner-normalized profiles of figure 18(*a*) are small in magnitude, this should not be interpreted to indicate that $\langle v\omega_z \rangle$ is dynamically insignificant. This point is clarified by considering the correlation coefficient, $R_{v\omega_z} = \langle v\omega_z \rangle/(v'\omega_z')$. Profiles of $R_{v\omega_z}$ are shown in figure 19(*a*,*b*). The profiles versus y^+ in figure 19(*a*) exhibit a variety of shapes with no readily apparent profile-to-profile trends. When plotted on the inertial domain (figure 19*b*), these profiles are better aligned such that they exhibit consistent behaviours. Near the beginning of this domain $R_{v\omega_z}$ varies between -0.15 and -0.25, and is in all cases a decreasing function of distance from the wall, except very near $y = \delta$. The profiles from the smooth and sandpaper surface flows are nearly parallel and exhibit a nominally logarithmic decrease. At their largest magnitudes these profiles attain values near -0.3 and -0.4, respectively. The profiles from the pea-gravel and bar roughness flows are also nearly parallel, but exhibit a downward concave curvature and respectively attain values near -0.5 and -0.6. Overall, the results of figure 19(*a*,*b*) reveal that the momentum sink-like mechanism associated with the $\langle v\omega_z \rangle$ correlation becomes increasingly efficient across layer IV.
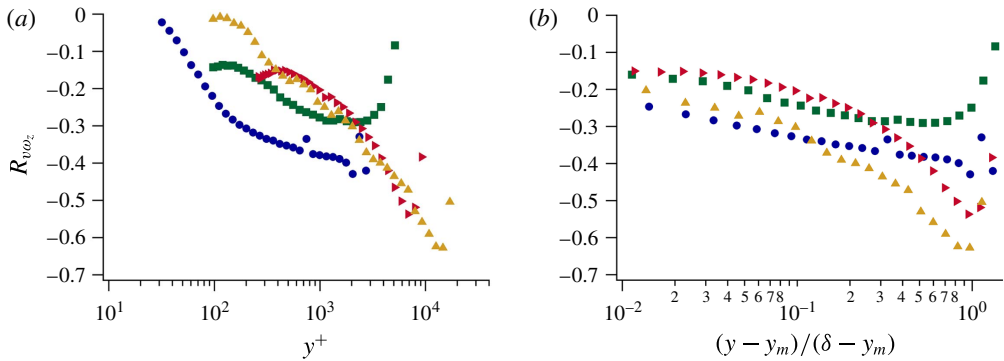
FIGURE 19. (Colour online) Profiles of the correlation coefficient $\langle v\omega_z \rangle/(v'\omega_z')$; (a) versus y^+, (b) versus $(y - y_m)/(\delta - y_m)$. Symbols same as in figure 6.

5.3.2. *Correlation maps and characteristic length scales*

Time delayed correlations of $v(t)$ and $\omega_z(t + \Delta t)$ as a function of y^+ and for varying Δt are useful for clarifying aspects of the flow structure underlying the $\Delta t = 0$ correlations of figure 18. These correlations also provide a convenient way to estimate a characteristic time (advected length) over which the v and ω_z motions interact.

For the correlation maps of figure 20, the time delay is converted to a streamwise length by invoking Taylor's hypothesis and using the local mean velocity. A number of features are apparent. One is that the correlations for the smooth wall and sandpaper roughness, and to a lesser extent the pea-gravel roughness, exhibit an asymmetric shape about $\Delta x = 0$. This behaviour was previously observed in smooth-wall flows at lower δ^+ (Monty *et al.* 2011*b*; Morrill-Winter & Klewicki 2013), and is demonstrated herein to persist for flows that exhibit approximate outer-layer similarity. In general, the maximum value of the correlation is not located at $\Delta x = 0$. Thus, the value of $\langle v\omega_z \rangle$ at any given y^+ position is sensitive to even small average phase shifts between the v and ω_z signals. Consistent with their respective profiles in figure 19(*b*), the relatively small k_s^+ sandpaper roughness correlation map retains the same qualitative shape as the smooth-wall map, but is nearly uniformly attenuated. Interior to $y/\delta \simeq 0.5$ the pea-gravel map has features that are similar to those exhibited by the smooth wall and sandpaper roughness flows. Beyond this region, it shows a rapid broadening of non-zero correlation that is more symmetrically distributed about $\Delta x = 0$. The bar roughness correlation map is distinctive in that non-zero correlation extends to much greater $\Delta x/\delta$ on either side of $\Delta x = 0$. For all wall-normal locations this correlation is symmetrically distributed about $\Delta x = 0$.

Per the method described in §4, streamwise correlation lengths, l_x, were computed from the correlation maps of figure 20. The inner-normalized profiles in figure 21(*a*) reveal that on the $y/\delta \lesssim 0.5$ portion of the inertial domain the l_x^+ values from the present smooth, sandpaper and pea-gravel flows show only a slight increase with roughness and Reynolds number. Over this domain, the profile for the bar roughness flow is nearly parallel to the others, but is shifted upward by about a factor of 5. Comparison of the lower δ^+ smooth-wall results from the studies of Monty *et al.* (2011*b*) and Morrill-Winter & Klewicki (2013) with the present smooth-wall profile indicates a small but consistent upward trend. (Note that the data of Morrill-Winter & Klewicki (2013) were doubled, since they used a single-sided definition of l_x.)
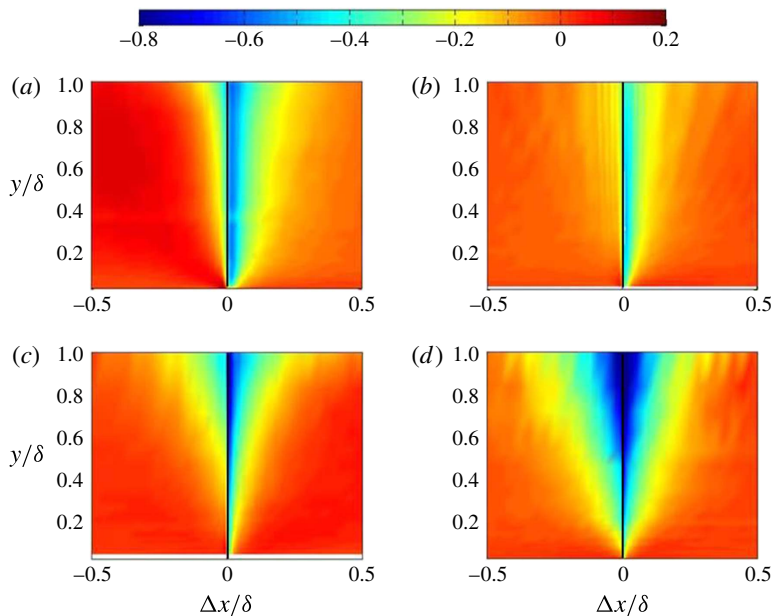
FIGURE 20. (Colour online) Correlation coefficient maps associated with $v(t)$ and $\omega_z(t + \Delta t)$, converted via Taylor's hypothesis to a spatial (Δx) correlation; (*a*) smooth wall, (*b*) sandpaper roughness, (*c*) pea-gravel roughness, (*d*) square bar roughness.

Figure 21(*b*) shows that the Reynolds number dependence of the smooth-wall flows is apparently removed when l_x is normalized by y_m. Note also that at the onset of the inertial domain all of the rough wall l_x/y_m values cluster between 0.6 and 0.9, while the smooth-wall profiles all have beginning values near $l_x/y_m = 2$. The bar roughness profile, however, increases more rapidly that the others near the start of the inertial domain, and by $(y - y_m)/(\delta - y_m) \simeq 0.1$ nominally merges with the smooth-wall profiles. Overall, the results of figure 21(*b*) suggest that, regardless of k_s^+ or δ^+, the value of l_x is $O(y_m)$ on the inertial domain. These results also suggest that roughness effects tend reduce l_x/y_m relative to the value found in smooth-wall flow.

5.4. *Spectral analysis*

Premultiplied frequency spectra of the v and ω_z time series were computed, and converted to streamwise wavelength spectra via Taylor's hypothesis. This section describes the resulting spectrograms, and provides an analysis of their characteristic wavelengths.

5.4.1. *v and ω_z spectrograms*

Contour maps depicting the premultiplied v spectra as a function of y/δ are given in figure 22(*a–d*). As with the observations of Morrill-Winter & Klewicki (2013), the present smooth-wall spectrogram shows a layer II concentration of spectral intensity over the range $200 \lesssim \lambda^+ \lesssim 600$ that is flat or slightly decreasing out to $y^+ \simeq y_m^+$, and then the median wavelength of the maximal intensity motions increases across layer IV. The sandpaper and smooth-wall spectrograms are quantitatively similar across the inertial domain. As might be expected, the pea-gravel and square bar v spectrograms
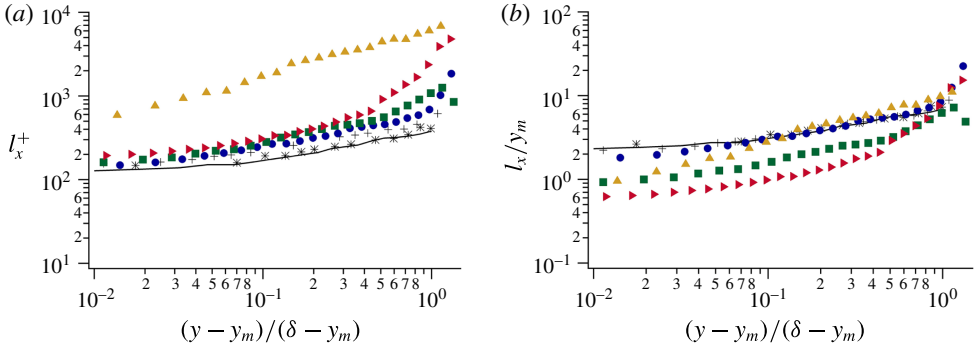
FIGURE 21. (Colour online) Inertial layer profiles of the characteristic length associated with the correlation between $v(t)$ and $\omega_z(t + \Delta t)$; (a) normalized by ν/u_τ, (b) normalized by y_m. Solid line derived from the $\delta^+ = 934$ channel DNS of Hoyas & Jimenez (2006), as presented in Monty *et al.* (2011b). Other symbols same as in figure 14.
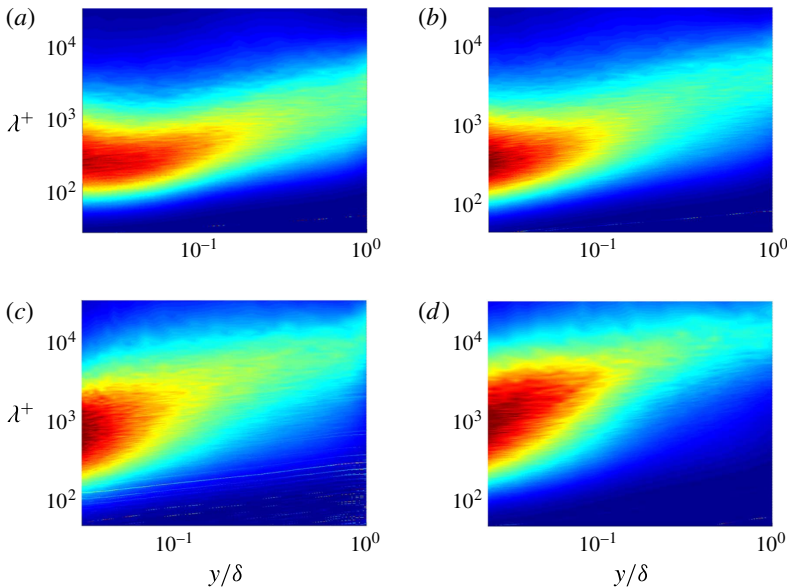

FIGURE 22. (Colour online) Premultiplied streamwise wavelength spectrogram of the wall-normal velocity fluctuations; (a) smooth-wall, (b) sandpaper roughness, (c) pea-gravel roughness, (d) square bar roughness.

exhibit considerably broader regions of concentrated spectral intensity, as well as an overall shift to larger wavelengths. They also show a monotonic increase across layer IV that is similar to that in the smooth-wall and sandpaper roughness flows. These behaviours are further quantified below.

Spectrograms of ω_z are shown in figure 23(a–d). The smooth-wall spectra are akin to the previous results of Morrill-Winter & Klewicki (2013) to the extent that across layer II the wavelength zone of maximal intensity is flat or slightly decreasing, and then across layer IV its centroid subtly shifts to larger wavelengths. As clarified below, these data also show some quantitative differences from previous smooth-wall
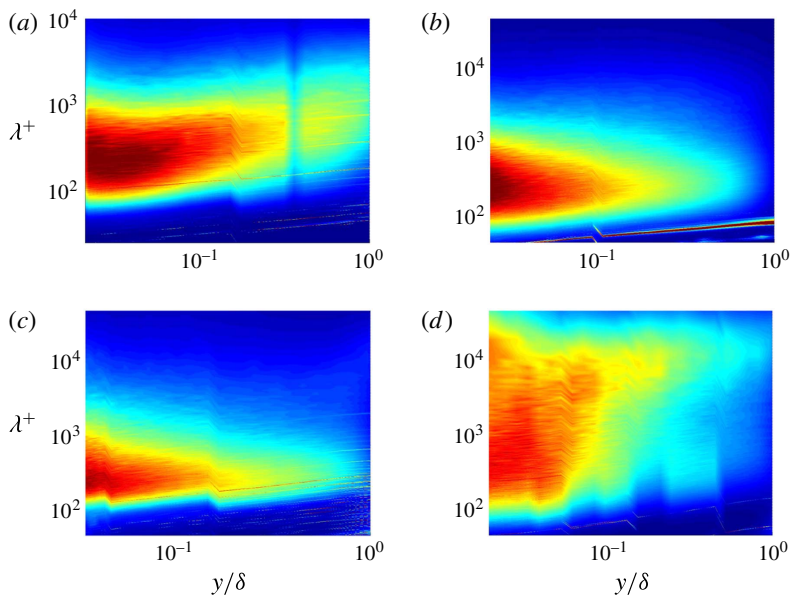
FIGURE 23. (Colour online) Premultiplied streamwise wavelength spectrogram of the spanwise vorticity fluctuations; (*a*) smooth-wall, (*b*) sandpaper roughness, (*c*) pea-gravel roughness, (*d*) square bar roughness.

measurements. Unlike the v spectra, the ω_z spectra from the sandpaper roughness flow exhibits a qualitative difference from the smooth-wall flow; demonstrating little increase in inner-normalized scale across layer IV. This feature is also characteristic of the pea-gravel spectra. The spectrogram for the square bar roughness is dramatically different from the others, exhibiting a broadband distribution of spectral intensity (spanning about two decades in wavelength) over most of the inertial domain.

5.4.2. *Peak wavelengths*

Peak wavelengths were extracted from the premultiplied v and ω_z spectra using the estimation method described in §4. These characteristic wavelengths are denoted λ_v and λ_ω, respectively.

Quantifying the trends noted in figure 22, the profiles of figure 24(*a,b*) indicate that λ_v generically follows an approximately logarithmic increase across the inertial domain, apparently regardless of k_s^+ or δ^+. Under the inner normalization of figure 24(*a*), the peak wavelengths of v exhibit an increasing trend with δ^+, or k_s^+ or both. Figure 24(*b*) clarifies the nature of these dependencies; evidencing that the variations of λ_v with Reynolds number and roughness are nominally the same as those exhibited by y_m. Here we also note that Morrill-Winter & Klewicki (2013) observed that for smooth-wall flows $\lambda_v \simeq \delta$ at $y \simeq \delta$ regardless of δ^+. Figure 24(*a*) indicates that this observation seems to also hold for the present smooth- and rough-wall flows. In combination with the result of figure 24(*b*), this finding suggests that from the beginning to the end of the inertial domain λ_v increases from $O(y_m)$ to $O(\delta)$, invariant of Reynolds number or roughness.

Inertial layer profiles of λ_ω are shown in figure 25. Under inner normalization (figure 25*a*), the smooth-wall profiles exhibit an increasing trend with increasing δ^+, but with the present data showing a larger increase than anticipated from the trend of
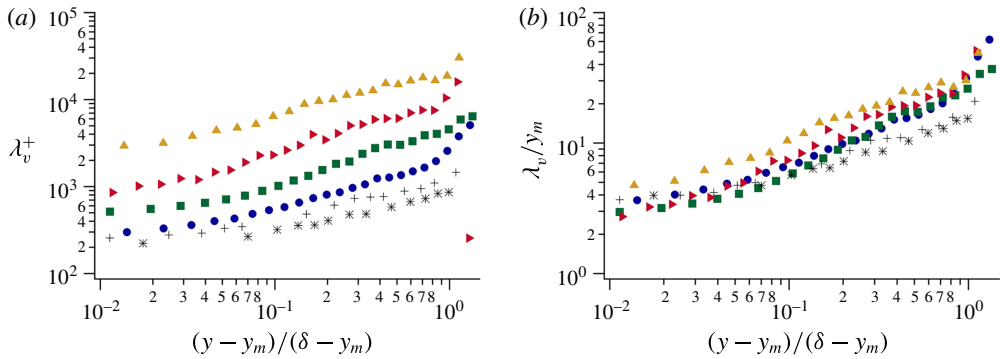
FIGURE 24. (Colour online) Inertial layer profiles of the characteristic wavelengths associated with the peaks in the premultiplied v spectra; (*a*) normalized by ν/u_τ, (*b*) normalized by y_m. Symbols same as in figure 14.
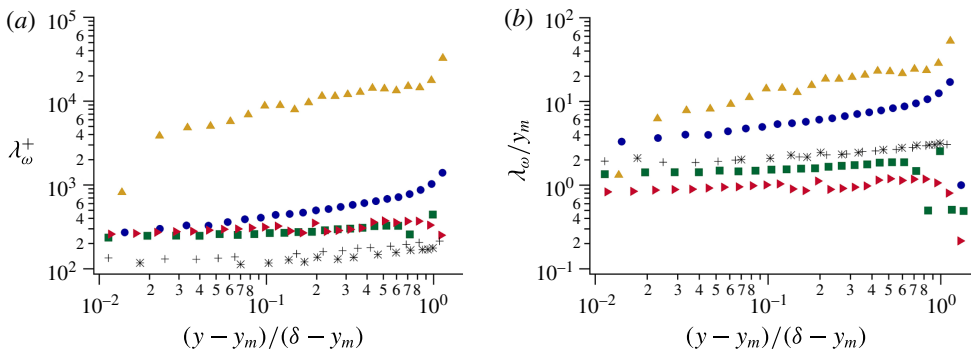

FIGURE 25. (Colour online) Inertial layer profiles of the characteristic wavelengths associated with the peaks in the premultiplied ω_z spectra; (*a*) normalized by ν/u_τ, (*b*) normalized by y_m. Symbols same as in figure 14.

the other smooth-wall profiles on the plot. The present smooth-wall data also exhibit an increasing trend with wall-normal distance that is greater than the very mild trend (if any) seen by the lower δ^+ profiles. In contrast, both the sandpaper and pea-gravel roughness λ_ω^+ profiles are essentially flat across the inertial layer, and are at the same inner-normalized scale of approximately 250 viscous units. The λ_ω^+ profile for the bar roughness flow is more than a decade larger than the other rough-wall profiles, and shows a noticeable increase with increasing in y. Unlike the λ_v profiles, figure 25(*b*) indicates that this size difference remains apparent when λ_ω is normalized by y_m. Under this normalization, the other rough wall $\lambda\omega/y_m$ profiles fall below the lower δ^+ smooth-wall profiles of Morrill-Winter & Klewicki (2013), as well as the present smooth-wall profile.

The ratio, λ_v/λ_ω, is a measure of the scale separation between these two variables, and inertial layer profiles of this ratio are shown in figure 26. For smooth-wall flow this ratio is expected to increase with increasing δ^+. As anticipated from the trends indicated in figures 24 and 25, however, the present smooth-wall profile falls below the lower δ^+ profiles on the plot. This is primarily because of the peak ω_z wavelength behaviours noted in figure 25(*a*). Relative to an outer region structure comprised of
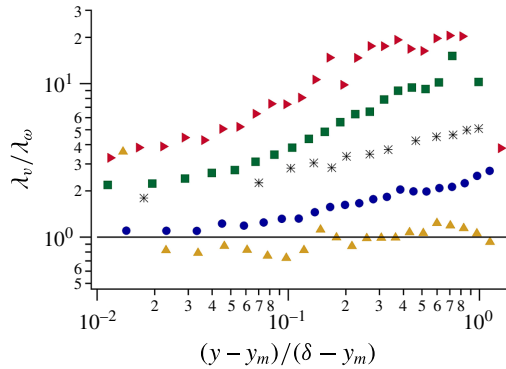
FIGURE 26. (Colour online) Inertial layer profiles of the ratio of the characteristic wavelengths associated with the peak in the premultiplied spectra of v and ω_z. Symbols same as in figure 14.

uniform momentum zones segregated by vortical fissures, λ_v/λ_ω is also expected to increase with increasing y. Here it is apparent that the distinctive attribute of the flow over the bar roughness is that $\lambda_v/\lambda_\omega \simeq 1$ everywhere, and thus the v and ω_z motions in this flow do not separate in scale across the inertial layer.

6. Discussion and conclusions

The present results lend support to the rough-wall extension of the theory described in § 2.2. Over a variety of roughness and Reynolds number conditions the extent of the linear region on the diagnostic plot was estimated to reside between $C_1 y_m \lesssim y \lesssim C_2 \delta$, where $C_1 \simeq 1.2$ and $C_2 \simeq 0.75$. Because the linear region identifies where u' and U exhibit (approximate) self-similarity, this finding agrees, in order of magnitude, with the proposed framework. Consistent with the results of Klewicki *et al.* (2015), the present analyses indicate that with roughness the upper boundary of the linear region extends to beyond the $y/\delta \simeq 0.5$ position found for smooth-wall flow (Zhou & Klewicki 2015). Part of the reason for the consistently larger y_e/δ values estimated herein is, however, attributable to the different method used to identify the extent of the linear region. The $S(u)$ zero-crossing data examined exhibit an apparent correlation with y_m, suggesting that this zero crossing marks the onset of the inertial domain regardless of k_s^+ or δ^+. $S(v)$ profiles also noticeably align when plotted versus y/y_m. The present results reinforce the scaling prediction that, near the onset of layer IV, $|\Omega_z| y_m / u_\tau$ is a value near unity independent of roughness or Reynolds number. When the $\langle \omega_z^2 \rangle$ profiles for the smooth, sandpaper and pea-gravel flows were similarly weighted using y_m, they also evidence invariance and alignment beginning near y_m.

Velocity statistics were generally found to be less sensitive to departures from Townsend's outer similarity hypothesis than ω_z statistics. (The linear portion of the diagnostic plot seems to constitute a particularly insensitive measure of outer similarity.) This connects to the conjecture of MKW13 that outer-layer similarity is, at best, only approximately met in rough-wall flows, because roughness essentially always leaves an imprint on the vorticity field motions. Indirect support for this was found in the divergent behaviour of the higher-order ω_z statistics for the smooth, sandpaper and pea-gravel flows, even though for these flows a number of statistics, including the $\langle \omega_z^2 \rangle$ profiles, exhibit approximate similarity on the inertial domain.

Conversely, the spanwise vorticity bearing motions in the square bar flow show an enhanced intensity on the inertial domain, and exhibit a disparate increase in scale. Furthermore, the $S(\omega_z)$ profile for this flow shows a clear positive excursion on layer IV, indicating that the most significant fluctuations are of sign opposite that of the mean vorticity. However, even with the noted increases in scale associated with roughness, the dynamics seem to inherently adjust such that the characteristic size of the inertial layer interactions between v and ω_z remains $O(y_m)$. Measurements covering greater k_s^+ and δ^+ ranges are needed to confirm the universality of this observation. Physically, this observation is consistent with the bulk of the momentum transport (and kinetic energy dissipation) being associated with the dynamics of $O(y_m)$ width vortical fissures, see figure 27. It also seems to be in accord with the similarity theory described by Davidson & Krogstad (2014). In the logarithmic layer of both smooth- and rough-wall flows, they found that low-order structure functions follow a logarithmic law as adjusted to account for local imbalances between turbulence kinetic energy production and dissipation. Significantly, they found that the y-scaling (associated with logarithmic dependence) derives from the decreasing dissipation rate with wall-normal distance.

The length scale analyses provided insights regarding the observed breakdown of outer similarity for the square bar flow. Here we first note that on the inner portion of the inertial domain the results of figure 21(b) show that the rate of increase of l_x/y_m is nearly the same for the smooth, sandpaper and pea-gravel flows. Thus, the more rapid increase of the l_x/y_m profile for the bar roughness flow is likely to connect to the observed violation of outer similarity in other statistics. Similarly, while the results of figure 24(b) indicate that, independent of k_s^+ or δ^+, the characteristic wavelengths of the v motions increase from $O(y_m)$ to $O(\delta)$ across layer IV, the ω_z motions in the bar roughness flow are markedly larger relative to y_m (figure 25b). This behaviour underlies the finding of figure 26 that the v and ω_z motions on layer IV of the bar roughness never scale separate. Physically, this suggests that the characteristic structure of uniform momentum zones segregated by narrow vortical fissures is significantly modified in this flow.

We conclude with a description of the present experimental observations within the context of the present theoretical framework. Figure 27(a,b) facilitate this by depicting mean dynamical features and vorticity field properties of smooth- and rough-wall flows, respectively. A number of mechanistic scenarios associated with roughness effects can be constructed that are consistent with the present framework. Here we focus on the three associated with (1.2). These connect to the structure of smooth-wall flow, and the breakdown of outer similarity.

In smooth-wall flow (figure 27a), there is an inherent scale at which the layer II vorticity field initiates its three-dimensionalization. Existing evidence suggests that this scale is $O(\sqrt{\nu\delta/u_\tau}) = O(y_m)$ (Morrill-Winter & Klewicki 2013). This feature bears some agreement with the thickened vortex sheet model proposed by Sreenivasan (1987), where he estimated a characteristic wavelength of the vortex sheet roll up to be $O(y_m)$. Across layer II scale separation between the velocity and vorticity field motions accompanies vorticity field three-dimensionalization, as caused by the mechanisms of stretching and reorientation. These processes subsequently lead to the formation of the vortical fissures. With the onset of the inertial domain, the leading mechanism for turbulent momentum transport (*TI* term) changes from $\langle w\omega_y \rangle$ (associated with vorticity stretching) to $\langle v\omega_z \rangle$ (associated with advective transport). The spatial dispersion of the vortical fissures across layer IV is consistent with the structure first revealed by Meinhart & Adrian (1995). The inception of this structural
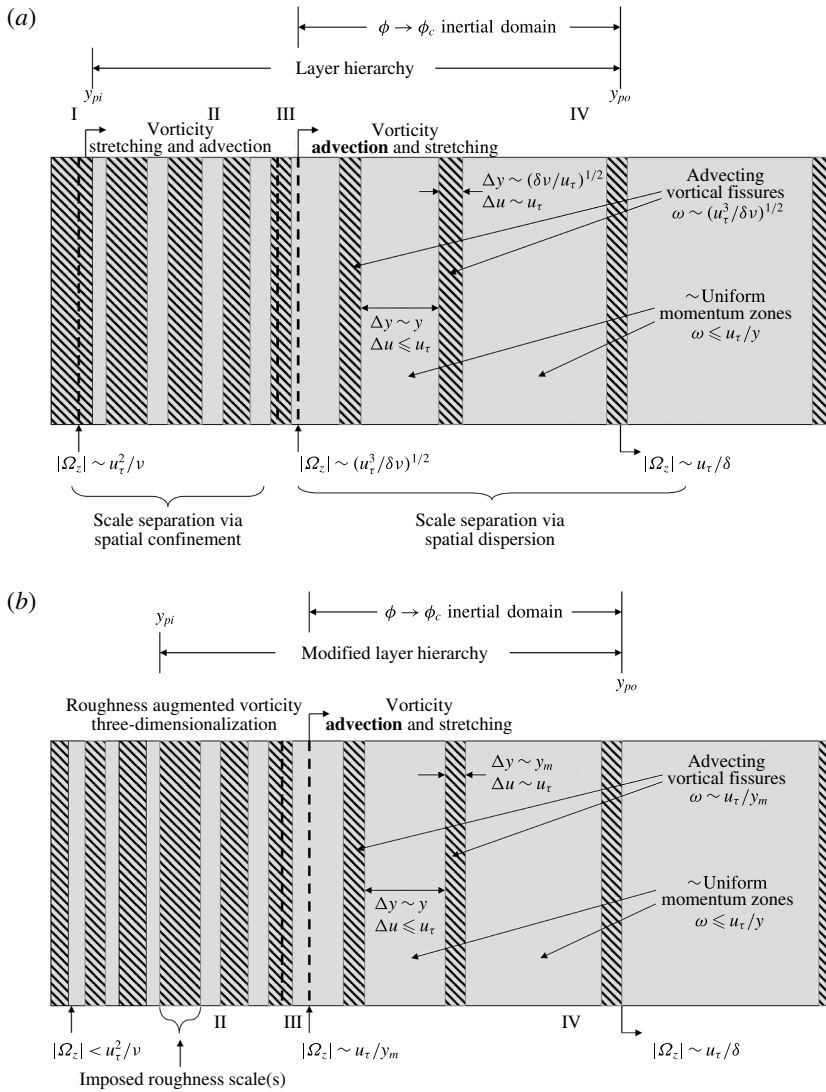
FIGURE 27. Schematic depiction of vorticity field attributes in (*a*) smooth-wall flows and (*b*) rough-wall flows for which $k_s \lesssim y_m$, adapted from Klewicki (2013*b*). Note that the horizontal scale is stretched (nominally logarithmic), e.g. in the smooth-wall flow layer II is only approximately 1.6 times wider than layer III. Velocity field motions (light grey) are space-filling throughout, while the vortically intense motions (hatched) spatially concentrate in layer II. These motions organize to form the vortical fissures characteristic of layer IV. In smooth-wall flow the layer II vorticity field three-dimensionalizes owing to the inherent vorticity stretching mechanisms. In rough-wall flow, the imposed roughness perturbation generally augments (possibly dominates) the vorticity field three-dimensionalization. Note that for smooth-wall flow $y_m \propto \sqrt{\nu\delta/u_\tau}$.

feature is also in accord with the rapid shift in the centroid of the mean vorticity distribution in the post-transitional flow, while the $O(\sqrt{\nu\delta/u_\tau}) = O(y_m)$ fissure width finds empirical support up to $\delta^+ = O(10^6)$ (Lighthill 1958; Klewicki, Ebner & Wu 2011; Klewicki 2013*b*).

We now consider how roughness modifies the process by which the layer II vorticity field three-dimensionalizes and forms (or fails to form) into fissures. When $k_s \ll y_m$, the imposed roughness scales constitute a relatively small perturbation to the inherent vorticity reorganization scale just described for smooth-wall flow. This, however, does not necessarily mean that k_s^+ is small. In general, such a perturbation is likely to generate a reduction in the subsequent correlation between v and ω_z on layer IV, and the present sandpaper flow results support this expectation. As $k_s \to y_m$, the scales of motion imposed by the roughness increasingly influence the dominant scales underlying layer II vorticity field three-dimensionalization. Here the roughness scale is expected to become an increasingly influential determinant of y_m. For increasing k_s/y_m, there is also likely to develop both a primary organization of the vorticity field (leading to fissure formation), as well as a cascade to vortical scales of motion smaller than those directly imposed by the roughness. Because they are imposed, sufficiently large roughness scales could lead to an intermittent internal structure to form within the fissures at Reynolds numbers much lower than such an internal structure might otherwise form in the smooth-wall flow (Klewicki 2013b). For the two cases just described, the layer II vorticity field undergoes three-dimensionalization sufficient to generate a scale-separated structure on layer IV that is qualitatively similar to what occurs solely as a function of δ^+ in smooth-wall flows. The present results suggest that a companion feature of outer similarity is scale separation between v and ω_z. This condition is approximately satisfied for the sandpaper and pea-gravel flows. Thus, the cases $k_s < y_m$ and $k_s \simeq y_m$ are nominally represented in figure 27(b).

When $k_s \gg y_m$, the process that otherwise leads to the uniform momentum zone/vortical fissure structure is qualitatively altered. Apparently, the size and two-dimensionality of the square bar roughness results in vorticity field motions that are resistant to the intrinsic stretching and reorientation mechanisms, and the scale separation between v and ω_z that coincides with the flows exhibiting outer similarity is thus never attained (figure 26). In this case, the structure on the inertial domain is qualitatively distinct from that depicted in figure 27.

Lastly, it is useful to reiterate that the present analysis used a single length, k_s, to characterize the roughness. Existing evidence indicates that this is a reasonable and pragmatic thing to do. Even supposing, however, that the present framework is conceptually flawless, a single length scale characterization of the inherently multi-scale perturbation imposed by roughness will lead to data scatter. Thus, at least some of the present scatter, for example in figure 9(b) or table 2, is rationally attributable to the use of k_s. Another source of data scatter comes from the estimation of y_m using the empirical correlations (1.2). Despite such scatter, it seems safe to surmise that those smooth- and rough-wall flows that (approximately) exhibit outer similarity share the properties of a layer II vorticity reorganization process that gives rise to scale separated inertial mean dynamics on layer IV. The present evidence suggests that the inertial layer quantitatively retains the uniform momentum zone/vortical fissure structure seen in four-layer regime smooth-wall flows.

Acknowledgement

REFERENCES

ALFREDSSON, P. H., SEGALINI, A. & ORLU, R. 2011 A new scaling for the streamwise turbulence intensity in wall-bounded turbulent flows and what it tells us about the 'outer peak'. *Phys. Fluids* **23**, 041702.

ANTONIA, R., ZHU, Y. & KIM, J. 1993 On the measurement of lateral velocity derivatives in turbulent flows. *Exp. Fluids* **15**, 65–69.

BRZEK, B., CAL, R. B., JOHANSSON, G. & CASTILLO, L. 2007 Inner and outer scalings in rough surface zero pressure gradient turbulent boundary layers. *Phys. Fluids* **19**, 065101.

CASTRO, B., SEGALINI & ALFREDSSON, P. H. 2013 Outer layer turbulence intensities in smooth- and rough-wall boundary layers. *J. Fluid Mech.* **727**, 119–131.

CHIN, C., PHILIP, J., KLEWICKI, J., OOI, A. & MARUSIC, I. 2014 Reynolds number dependent turbulent inertia and onset of log-region in pipe flows. *J. Fluid Mech.* **757**, 747–769.

CONNELLY, J. S., SCHULTZ, M. P. & FLACK, K. A. 2006 Velocity-defect scaling for turbulent boundary layers with a range of relative roughness. *Exp. Fluids* **40** (2), 188–195.

DAVIDSON, P. A. & KROGSTAD, P. A. 2014 A universal scaling for low-order structure functions in the log-law region of smooth- and rough-wall boundary layers. *J. Fluid Mech.* **752**, 140–156.

DEGRAAFF, D. B. & EATON, J. K. 2000 Reynolds number scaling of the flat-plate turbulent boundary layer. *J. Fluid Mech.* **422**, 319–346.

DJENIDI, L., ANTONIA, R. A., AMIELH, M. & ANSELMET, F. 2008 A turbulent boundary layer over a two-dimensional rough wall. *Exp. Fluids* **44**, 37–47.

DUVVURI, S. & MCKEON, B. J. 2015 Triadic scale interactions in a turbulent boundary layer. *J. Fluid Mech.* **767**, R4-1.

EBNER, R. 2014 Influences of roughness on the inertial mechanism of turbulent boundary-layer scale separation. PhD Dissertation, University of New Hampshire, Durham, New Hampshire, USA.

EFROS, V. & KROGSTAD, P-.Å. 2011 Development of a turbulent boundary layer after a step from smooth to rough surface. *Exp. Fluids* **51**, 1563–1575.

FIFE, P., KLEWICKI, J., MCMURTRY, P. & WEI, T. 2005 Multiscaling in the presence of indeterminacy: wall-induced turbulence. *Multiscale Model. Simul.* **4**, 936–959.

FIFE, P., KLEWICKI, J. & WEI, T. 2009 Time averaging in turbulence settings may reveal an infinite hierarchy of length scales. *J. Discrete Continuous Dyn. Syst.* **24**, 781–807.

FLACK, K. A., SCHULTZ, M. P. & SHAPIRO, T. A. 2005 Experimental support for Townsend's Reynolds number similarity hypothesis on rough walls. *Phys. Fluids* **17**, 035102.

FOSS, J. F. & HAW, R. 1990 Transverse vorticity measurements using a compact array of four sensors. *ASME FED* **97**, 71–76.

FUKAGATA, K., IWAMOTU, K. & KASAGI, N. 2002 Contributions of Reynolds stress distribution to the skin friction in wall-bounded flows. *Phys. Fluids* **14**, L73–L76.

HANSEN, A. 1964 *Similarity Analysis of Boundary Value Problems in Engineering*. Prentice-Hall.

HAUPTMAN, Z. 2010 Characterization of a low-speed boundary layer wind tunnel. MS thesis, University of New Hampshire, Durham, New Hampshire, USA.

HONG, J., KATZ, J. & SCHULTZ, M. P. 2011 Near-wall turbulence statistics and flow structures over three-dimensional roughness in a turbulent channel flow. *J. Fluid Mech.* **667**, 1–37.

HOYAS, S. & JIMENEZ, J. 2006 Scaling the velocity fluctuations in turbulent channels up to $Re_\tau = 2003$. *Phys. Fluids* **18**, 011702.

HUTCHINS, N., NICKELS, T. B., MARUSIC, I. & CHONG, M. S. 2009 Hot-wire spatial resolution issues in wall-bounded turbulence. *J. Fluid Mech.* **635**, 103–136.

JIMÉNEZ, J. 2004 Turbulent flows over rough walls. *Annu. Rev. Fluid Mech.* **36**, 173–196.

KLEWICKI, J. C. & FALCO, R. E. 1990 On accurately measuring statistics associated with small-scale structure in turbulent boundary layers using hot-wire probes. *J. Fluid Mech.* **219**, 119–142.

KLEWICKI, J. C., GENDRICH, C. P., FOSS, J. F. & FALCO, R. E. 1990 On the sign of the instantaneous spanwise vorticity component in the near-wall region of turbulent boundary layers. *Phys. Fluids* A **2**, 1497–1501.

KLEWICKI, J. C. 1997 Self-sustaining traits of near-wall motions underlying boundary layer stress transport. In *Self-Sustaining Mechanisms of Wall Turbulence* (ed. R. Panton), pp. 135–166. Computational Mechanics Publications.

KLEWICKI, J. 2013*a* Self-similar mean dynamics in turbulent wall flows. *J. Fluid Mech.* **718**, 596–621.

KLEWICKI, J. 2013*b* A description of turbulent wall-flow vorticity consistent with mean dynamics. *J. Fluid Mech.* **737**, 176–204.

KLEWICKI, J., EBNER, R. & WU, X. 2011 Mean dynamics of transitional boundary layer flow. *J. Fluid Mech.* **682**, 617–651.

KLEWICKI, J., MORRILL-WINTER, C. & ZHOU, A. 2015 Inertial logarithimic layer properties and self-similar mean dynamics. In *Proceedings of Turbulent Shear Flow Phenomena 9*; paper no. 188, University of Melbourne.

KROGSTAD, P-.Å. & ANTONIA, R. A. 1999 Surface roughness effects in turbulent boundary layers. *Exp. Fluids* **27** (5), 450–460.

LIGHTHILL, M. J. 1958 On displacement thickness. *J. Fluid Mech.* **4**, 383–392.

LIGRANI, P. & MOFFAT, R. 1986 Structure of transitionally rough and fully rough turbulent boundary layers. *J. Fluid Mech.* **162**, 69–98.

MARUSIC, I., MONTY, J., HULTMARK, M. & SMITS, A. 2013 On the logarithmic region in wall turbulence. *J. Fluid Mech.* **716**, R3–11.

MATHIS, R., MARUSIC, I., HUTCHINS, N. & SREENIVASAN, K. R. 2011 The relationship between the velocity skewness and the amplitude modulation of the small scale by the large scale in turbulent boundary layers. *Phys. Fluids* **23**, 121702.

MEINHART, C. & ADRIAN, R. J. 1995 On the existence of uniform momentum zones in turbulent boundary layers. *Phys. Fluids* **7**, 694–696.

MEHDI, F. 2012 Mean force structure and scaling of rough-wall turbulent bound ary layers. PhD Dissertation, University of New Hampshire, Durham, New Hampshire, USA.

MEHDI, F., KLEWICKI, J. & WHITE, C. 2010 Mean momentum balance analysis of rough-wall turbulent boundary layers. *Physica* D **239**, 1329–1337.

MEHDI, F., KLEWICKI, J. & WHITE, C. 2013 Mean force structure and its scaling in rough-wall turbulent boundary layers. *J. Fluid Mech.* **731**, 682–712.

MEHDI, F. & WHITE, C. 2011 Integral form of the skin friction coefficient suitable for experimental data. *Exp. Fluids.* **50**, 43–51.

MENEVEAU, C. & MARUSIC, I. 2013 Generalized logarithmic law for high-order moments in turbulent boundary layers. *J. Fluid Mech.* **719**, R1–11.

METZGER, M. M. & KLEWICKI, J. C. 2001 A comparative study of near-wall turbulence in high and low Reynolds number boundary layers. *Phys. Fluids* **13**, 692–701.

MEYERS, T., FOREST, J. B. & DEVENPORT, W. J. 2015 The wall-pressure spectrum of high-Reynolds-number turbulent boundary-layer flows over rough surfaces. *J. Fluid Mech.* **768**, 261–293.

MONTY, J. P., ALLEN, J. J., LIEN, K. & CHONG, M. S. 2011*a* Modification of the large-scale features of high Reynolds number wall turbulence by passive surface obtrusions. *Exp. Fluids* **51**, 1755–1763.

MONTY, J. P., KLEWICKI, J. C. & GANAPATHISUBRAMANI, B. 2011*b* Characteristics of momentum sources and sinks in turbulent channel flow. In *Proceedings of Turbulent Shear Flow Phenomena 7*; paper no. IC4P, University of Ottawa.

MORRILL-WINTER, C. & KLEWICKI, J. 2013 Influences of boundary layer scale separation on the vorticity transport contribution to turbulent inertia. *Phys. Fluids* **24**, 015108.

MURLIS, J., TSAI, H. M. & BRADSHAW, P. 1982 The structure of turbulent boundary layers at low Reynolds numbers. *J. Fluid Mech.* **122**, 13–56.

PRIYADARSHANA, P. J. A., KLEWICKI, J. C., TREAT, S. & FOSS, J. F. 2007 Statistical structure of turbulent-boundary layer velocity-vorticity products at high and low Reynolds numbers. *J. Fluid Mech.* **570**, 307–346.

RAJAGOPALAN, S. & ANTONIA, R. A. 1993 Structure of the velocity field associated with the spanwise vorticity in the wall region of a turbulent boundary layer. *Phys. Fluids* A **5**, 2502–2510.

RAUPACH, M. R., ANTONIA, R. A. & RAJAGOPALAN, S. 1991 Rough-wall boundary layers. *Appl. Mech. Rev.* **44**, 1–25.

SAHA, S., KLEWICKI, J., OOI, A. & BLACKBURN, H. 2015 On scaling pipe flows with sinusoidal transversely-corrugated walls: analysis of data from the laminar to low Reynolds number turbulent regime. *J. Fluid Mech.* **779**, 245–274.

SCHLATTER, P. & ORLU, R. 2010 Assessment of direct numerical simulation data of turbulent boundary layers. *J. Fluid Mech.* **659**, 116–126.

SCHULTZ, M. P. & FLACK, K. A. 2007 The rough-wall turbulent boundary layers from the hydraulically smooth to the fully rough regime. *J. Fluid Mech.* **580**, 381–405.

SREENIVASAN, K. R. 1987 A unified view of the origin and morphology of the turbulent boundary layer structure. In *Turbulence Management and Relaminarization* (ed. H. W. Liepmann & R. Narasimha), pp. 37–60. Springer.

TENNEKES, H. & LUMLEY, J. L. 1972 *A First Course in Turbulence*. MIT Press.

TOWNSEND, A. 1976 *The Structure of Turbulent Shear Flow*. Cambridge University Press.

TROPEA, C., YARIN, A. & FOSS, J. F. (Eds) 2007 *Handbook of Experimental Fluid Mechanics*. Springer.

VINCENTI, P., KLEWICKI, J., MORRILL-WINTER, C., WHITE, C. & WOSNIK, M. 2013 Streamwise velocity statistics in turbulent boundary layers that spatially develop to high Reynolds number. *Exp. Fluids* **54**, 1629–1638.

VOLINO, R. J., SCHULTZ, M. P. & FLACK, K. A. 2011 Turbulence structure in boundary layers over periodic two- and three-dimensional roughness. *J. Fluid Mech.* **676**, 172–190.

WEI, T., FIFE, P., KLEWICKI, J. & MCMURTRY, P. 2005 Properties of the mean momentum balance in turbulent boundary layer, pipe and channel flows. *J. Fluid Mech.* **522**, 303–327.

ZHOU, A. & KLEWICKI, J. 2015 Properties of the streamwise velocity fluctuations in the inertial layer of turbulent boundary layers and their connection to self-similar mean dynamics. *Intl J. Heat Fluid Flow* **51**, 372–382.